8-22-2016

Sensitivity studies on the shear lag parameter β using analytical and numerical techniques

George Thomas Avery
Rowan University

SENSITIVITY STUDIES ON THE SHEAR LAG PARAMETER β USING ANALYTICAL AND NUMERICAL TECHNIQUES

by

George T. Avery

A Thesis

Submitted to the
Department of Mechanical Engineering
College of Engineering
In partial fulfillment of the requirement
For the degree of
Master of Science in Mechanical Engineering
at
Rowan University
July 18, 2016

Thesis Chair: William T. Riddell, Ph.D.

Acknowledgements

I would like to express my appreciation to Dr. William Riddell for taking me in as one of his graduate students and guiding me through my research. It is because of him that I have the intellectual tools to give me an edge in whatever career I pursue. I would also like to thank my friends and family for supporting me through the last two years.

Abstract

George Avery
SENSITIVITY STUDIES ON THE SHEAR LAG PARAMETER β USING ANALYTICAL AND NUMERICAL TECHNIQUES
2015-2016
William T. Riddell, Ph.D.
Master of Science in Mechanical Engineering

The strength of fiber-reinforced composites is dependent on the strength of the fiber-matrix interface bond. Thermal, chemical, and other means have been used to modify the surface of fibers, resulting in increased fiber-matrix interface bond strength. However, researchers are still dependent on empirical methods to relate surface modifications to composite performance. Additional efforts are required to develop physics-based models for micro-mechanical effects on interfacial bond strength that will be needed for the improved design and processing of fiber reinforced composites. It is anticipated that experimental, numerical, and analytical efforts will be needed to contribute toward this endeavor.

A numerical approach is presented in this thesis that allows the shear lag parameter, β, to be extracted from finite element results. Extracting the shear lag parameter from numerical data allows numerical and analytical approaches to be compared. Axisymmetric finite element analyses of fiber pull out, axisymmetric macrobond, and fully embedded fiber fracture tests are discussed in light of this approach. Material and geometric properties used in numerical models are then varied to study their effects on the fitted value of β. It is anticipated that this approach will enable and enhance future research efforts to simulate the effect of fiber surface texture on pull out strength.

Table of Contents

List of Figures

Chapter 1

Introduction

Increasing demand for high performance and low operating cost in products has led to an increased demand for high strength to weight and high stiffness to weight ratios for materials systems. This demand has led to the development and adoption of fiber-reinforced composite systems, where strong and stiff fibers are embedded in a lighter, but weaker matrix material. Typical examples of fiber reinforced composite material systems are glass fiber-reinforced, carbon fiber-reinforced and aramid fiber-reinforced polymer composites. The strength of fiber-matrix composites is largely governed by the interfacial bond strength between the fiber and the matrix, rather than the strength of either the fiber or matrix materials individually. Therefore, many efforts to improve the strength of fiber matrix composites have focused on improving this bond strength. Unfortunately, despite experimental, theoretical and numerical efforts, the transfer of loads from matrix to fiber through interfacial shear is still not well understood.

The goal of this thesis is to explore the relationships between a theoretical shear lag model, and results from finite element approaches. Predictions from these models are compared to published experimental data, where appropriate. The approach and subsequent results are broken up into several chapters. Previous efforts to understand the material properties of fiber composites including analytical, experimental, and numerical approaches are further discussed in chapter 2. The approach used to conduct the research described by this thesis is outlined in chapter 3. The shear-lag based analytical solution to the stress transfer of different experimental cases is described in chapter 4, while the

numerical FEA approach is outlined in chapter 5. These two methods are then compared for the purposes of optimizing the shear lag parameter β, which allows for the interpretation of the rate of stress transfer between the fiber and matrix in the composite. This is accomplished using several methods discussed in chapter 6. With a method of extracting a β value we can better understand how material properties along with certain geometric properties of a pull-out test can affect the stress transfer within a composite. Chapter 7 show how the ratio of Young's modulus along with fiber embedment length and test grip location can affect β. Chapter 8 then takes these parameters and then sets them to match certain published experiments to see if the published data can be replicated through modeling. A discussion of how the best fit value of β, along with the methods of determining the best fit β change between the different boundary conditions expressed in chapter 3 and the parameters studied in chapter 7 is held in chapter 8.

Chapter 2

Literature Review

The strength of fiber composites can be greatly influenced by the strength of the bond between the fiber and the matrix material. As this bond strengthens, the amount of load that a composite can withstand increases. An added benefit to this method is that existing composite configurations can be enhanced instead of spending energy and resources developing new materials to accomplish the same task. In an effort to strengthen this bond, surface treatments have been used to alter the fibers being embedded in the composite. The treatments include but are not limited to exposure to chemical baths [1] or UV radiation [2,3]. The objective of these treatments is to increase surface roughness to allow an increase in surface area for the resin of the matrix to adhere to.

Unfortunately, the work needed to analyze the effectiveness of various surface treatments can be time consuming and costly. Currently, the effectiveness of surface treatments on fibers is evaluated using experimental approaches. These experiments include measuring the force needed to debond an exposed fiber from a droplet of matrix material. These tests can take the form of microdroplet tests as performed by Miller *et al.* [4] Nishikawa *et al*. [5] and Cen *et al*. [6]. These tests can also be performed with a large amount of matrix material which are known as macrodroplet or macrobond tests. Examples of this method are found in the work by Piggot *et al.*, [7] and Takaku *et al.*, [8] and Hann *et al*. [9]. The majority of these experiments are conducted by pulling the fiber through a rigid plate or knife edges creating a top fixity boundary condition for

displacement. Bottom fixity conditions are also used by Tsai *et al*. [10] and partly by Brandstetter *et al*. in their study of fiber bundles as opposed to single fiber experiments [11]. Fragmentation tests such as those performed by Bannister *et al*. [12], and Galiotis *et al*. [13] fully embed the fiber in a matrix coupon. Examples of these test geometries can be seen in figure 1. Note that the geometric constraints are not shown, as these are different for different test configurations.

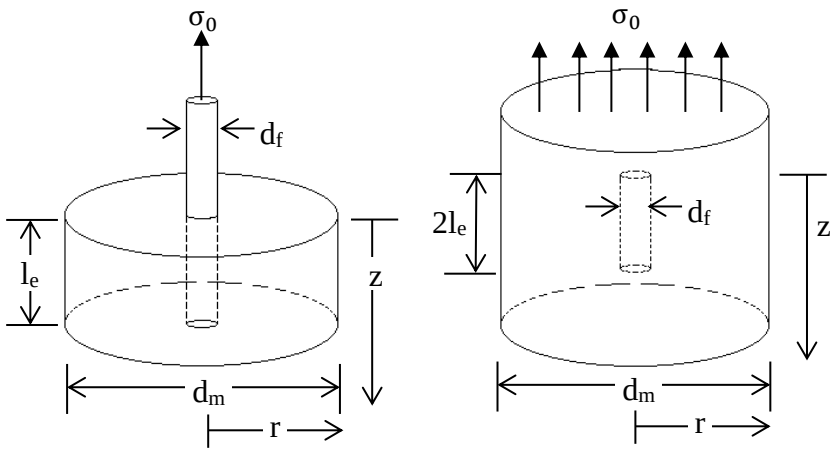

Figure 1. Concentric cylinder model for exposed (microdroplet, macrobond, pull-out tests) and fully embedded fibers (fragmentation tests)

In addition to measuring debond force, Raman spectroscopy can be used to measure internal stress within the composite. Through Raman spectroscopy [14], stress concentrations can be measured by the scattering of light by molecular vibrations induced by loading. The magnitude of the scattering corresponds to a specific stress concentration within the material being studied. In addition to measuring debond force, the various forms of pull out and fragmentation tests can measure the strength of the composite after the fibers have begun to debond from the matrix material. Multiple

iterations of these tests must be performed to characterize the effect of various surface treatment parameters, making the process of finding an ideal surface treatment a long and expensive process. Raman spectroscopy can also be costly since it requires high quality sensors and light sources to ensure accurate measurements of the sensitive shifts in the Raman peak [14]. Another hindrance of pull out tests is that aside from the use of Raman spectroscopy, the results come in the form of load vs displacement. Stress behavior must then be inferred by converting the load transfer into stress transfer throughout the composite.

To better understand the behavior of surface treatments on composite materials a simplified model can be analyzed to understand the general behavior of stress along the fiber interface. Stress transfer [15,16] and energy release rate [17,18] are two concepts with analytical solutions that have been developed to characterize composite behavior and the overall debond force. The shear lag theory can be implemented by either using an approach which can be solved to be based on either the far field strain in the composite [13,19,20] or by using the far field stress acting on the fiber [11,16,21]. These two solutions are similar and are separated by the far field term. Hooke's law relates stress and strain which in turn relates the two solutions. The analytical method discussed in this paper is a form of the stress-based shear lag method first developed by Cox in 1952 [21], who presented a governing equation for the average axial stress of a fiber embedded in a matrix. This governing equation has been found to be applicable to many different pull out scenarios through slight modifications that are dependent on the configuration. The shear lag method is a way to analytically model the uneven stress distribution of an object under load that is partially anchored to or within a rigid body. In

his solution Cox uses a parameter β which quantifies the fiber's ability to transfer load to the matrix and is a function of material properties and the volumetric fractions of the fiber and matrix. Cox's original equation for the shear lag parameter β was modified by Nayfeh [22]. The value of β has also been shown to be sensitive to the geometry of the experiment beyond the volume fractions [23-25]. Furthermore, there is a limited range of volume fractions for which the analytical solutions agree with experimental results [18]. To overcome these sensitivities, Zhandarov *et* al. [24] and Holsman *et* al. [26] have used β as a fitting parameter to match experimental results instead of directly solving for it. This has been accomplished by considering trends in average shear stress versus embedment length that are predicted by shear lag models, and identifying the values of both of ultimate shear stress and β that allow for the best agreement with experimentally observed trends in the average shear stress at delamination vs embedment length, as well as fitting fiber strains measured using Raman spectroscopy [13]. In this approach the ultimate interfacial shear strength (IFSS) is the value of the curve at l_e=0, and β determines the slope of the curve. The values are changed until a minimal error is achieved between the best fit curve and the experimental data. However, this process requires the use of pull out experiments, denying an independent analytical solution. Another disadvantage to this method is that the analytical interpretation for the stress transfer along the fiber/matrix interface falls short of the stress concentration that occurs where the fiber meets the matrix material.

A more popular method of measuring and predicting stress and load behavior along the fiber interface is the use of finite element programs. Through this method, debonding in composites can be modeled allowing numerical solutions to fiber pull-out

experiments. Hutchinson *et al*. [27], Lin *et al*. [28], and Tsai *et al*. [29] among others have used finite element models to study fiber debond. The use of this method is attractive because computer models can be adapted to analyze the behavior of a wide range of geometries. Yang *et al*. [30] use FE modeling to determine effects of embedment length and matrix radius on the stress in a composite. Numerical modeling also allows for the detailed study of internal stresses. Marotzke [31] uses a FEA to calculate the far stress fields and concentrations in different composite geometries. Computational efficiency can be further increased by the use of axisymmetrical elements [32]. This method considers a two dimensional cross-section of the geometry being studied and then revolves the geometry around a central axis of symmetry. This allows for a three-dimensional analysis with considerably less computational time, but requires axial symmetry. The axis of symmetry also simplifies the boundary conditions needed to execute the study. Another advantage of computer modeling is that the stress concentrations at the start and end of the fiber/matrix interface can be more precisely modeled than by using a shear lag approach. The shear lag approach does not capture these stress concentrations due to certain assumptions *i.e.* no radial displacement and no transverse stresses [16]. Marotzke [25] shows how changes in analytical boundary conditions corresponding to the fiber ends can affect the agreement between shear lag and FEA solutions while Zhao *et al*. [19] shows how refinements to previous assumptions can make the shear lag method more robust. When modeling damage, computer models for debonding in composites must use analytical interpretations of how the fiber displaces within the matrix *i.e.* cohesive zones or frictional models. Chen *et al*. [33] use a bilinear cohesive traction-separation law to model both the linear and nonlinear regimes of the

composite. Hutchinson *et al*. [27] and Lin *et al*. [28] use a friction based models to allow debonding where Tsai *et al*. [29] use a mixture of cohesive zones and friction models. Modeling outside the linear elastic region of a composite requires a general knowledge of how the materials being modeled will behave ahead of time for an accurate model to be created, limiting the exploratory nature of the FEA method.

Chapter 3

Approach

The goal of this work is to better understand the transfer of stress between the fiber and matrix during different loading scenarios. This understanding will be developed by combining solutions from both analytical and numerical approaches. To accomplish this, analytical results based on shear lag analysis and FEA results are compared for two different configurations that are intended to represent pull-out and fragmentation experiments. The analytical and numerical models are limited to linear elastic behavior that occurs prior to any damage in the fiber, matrix, or the fiber-matrix interface. All cases are assumed to be isotropic and have perfect bonds between the fiber and matrix. No efforts to model delamination or failure are made in either the analytical or numerical models.

The shear lag solution used in this paper uses concentric circle geometries to simplify the geometries of the experiments being modeled. Figure 2 shows the different boundary conditions imposed on the two concentric circle models. Figure 2 shows that for any configuration, only one end of a configuration is fixed and the other end is free. The first concentric circle configuration modeled is the single exposed fiber. The main feature of this configuration is that the fiber is exposed at one or both ends of the matrix material. Two different boundary conditions were studied for this test configuration. The first boundary condition is that of a pull-out test where the bottom of the fiber and matrix cylinders are anchored to a rigid surface leaving the rest of the geometry free. A specified load is then applied to the top surface of the fiber.

The second set of boundary conditions used are those of a macrobond test. In this configuration the load is in the same location as the previous configuration. However, the top of the matrix cylinder is now held in place by a rigid plate attached to the matrix by rollers placed a specified distance away from the fiber. This boundary condition is similar to the rigid plate used to anchor the experiments performed by Holsman *et al*. and leaves the bottom of the fiber and matrix as free surfaces.

The second concentric circle configuration modeled is that of the fragmentation test. For this case the fiber is fully embedded in the matrix and is no longer exposed. The bottom surface of the matrix is fixed to a riged surface while a specified load is placed on the top surface. All cases are modeled as axisymmetric. The axis of symmetry ensures that the center of all specimens is fixed against translation in the r-direction allowing the use of roller boundaries exclusively. These geometries and boundary conditions are further illustrated and explained in chapter 5.

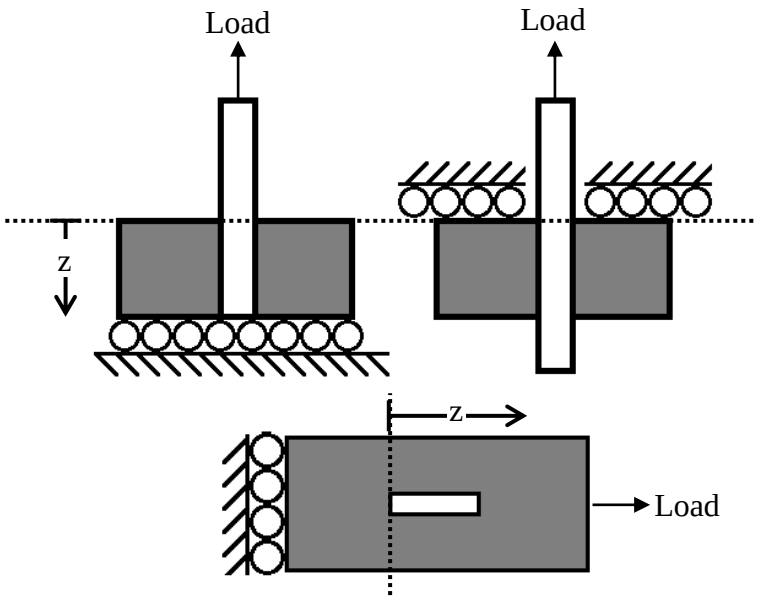

Figure 2. Boundary conditions for a) pull-out test, b) macrobond test, *c*) fragmentation test

Three parameters are used to characterize these configurations. The first parameter is based upon material properties and is the ratio of the Young's modulus of the fiber to that of the matrix' denoted as λ where

$$\lambda=\frac{E_f}{E_m} \tag{1}$$

The other two parameters are geometric and describe the embedment length of the fiber and the distance from the fiber surface to the macrobond roller boundary (hole radius). Embedment length is denoted as l_e which is normalized by the diameter of the embedded fiber d_f. The normalized embedment length is denoted as γ where

$$\gamma=\frac{l_e}{d_f} \tag{2}.$$

The hole diameter is denoted as d_h which is also normalized by the diameter of the fiber d_f. The normalized hole diameter is denoted as α where

$$\alpha=\frac{d_h}{d_f} \tag{3}.$$

The ratio of hole diameter to fiber diameters applies to only the macrobond test and does not exist in the case of the fragmentation tests.

For each scenario the corresponding shear lag and FEA solutions will be compared. The shear lag parameter β first proposed by Cox describes the efficiency of the fiber to transfer load to the composite. Cox's equation for β has later been modified by Nayfeh [22]. In addition to the analytical solution to β, a value exists that allows for a best fit between both shear lag and FEA solutions. The revised β by Nayfeh is considered in this thesis and is defined as

$$\beta = \left[\frac{2}{\left(\frac{d_f}{2}\right)^2 E_f E_m} \left(\frac{E_f V_f + E_m V_m}{\frac{V_m}{4G_f} + \frac{1}{2G_m}\left(\frac{1}{V_m}\ln\frac{1}{V_f} - 1 - \frac{V_f}{2}\right)} \right) \right]^{1/2} \quad (4)$$

and has units of 1/length. β controls the rate at which the stress is transferred from the fiber to the matrix.

In this thesis β will be used as a fitting parameter, but will be calculated without the use of experimental debond forces. A shear lag derivation for axial and shear stress as a function of *z* will be compared to FEA solutions using a least squares fit. By changing the value of β we can change the slope of the shear-lag based solution until the shear lag model achieves a best fit agreement with the corresponding FEA. This comparison will allow us to calculate an optimized value for β for a given test geometry. Once optimized, β will then be normalized by the diameter of the fiber d_m and denoted as *C*, where

$$C = \frac{\beta d_f}{2} \quad (5)$$

A range of different geometric and material properties will be used to analyze the sensitivity of *C*. These results will then be compared to experimentally fitted values. The goal is to have both numerical and analytical solutions work together to create a strong solution for the value of β and therefore the internal stress behavior of the composite.

Chapter 4

Shear Lag Theory

A type of single fiber macrobond and pull out tests, as well as fragmentation tests were analyzed in this study. In these cases, a single fiber is surrounded by a matrix material modeled by the concentric circle configuration. In both cases of the single exposed fiber the outer surface of the fiber is free before entering the matrix material. The approach developed for the case of an exposed fiber is then modified for fragmentation tests. For this case, the concentric circle model is expanded to include a fully embedded fiber. These scenarios are best analytically characterized by the shear lag method of problem solving. Shear lag solutions can take several forms. The relationships developed by Cox [21] were used to solve for the average axial stress $\langle\sigma_f\rangle$ and interfacial shear stress τ as a function of location along the z axis. The fiber in the test geometry is characterized by its diameter d_f, embedment length l_e, and its Young's modulus E_f and Poisson's ratio v_f. The matrix material is characterized by its diameter d_m, and Young's modulus E_m and Poisson's ratio v_m. Both materials were treated as isotropic and homogenous.. A range of λ was studied by changing the Young's modulus of the fiber while E_m v_m and v_f were held constant throughout the study.

Exposed Single Fiber

In figure 1 an axial load is placed on the free fiber end of the exposed fiber configuration creating an average axial stress $\langle\sigma_0\rangle$ in the free portion of the fiber. Note that the brackets are used to represent an average value over a given cross section of the fiber. In the portion of the fiber that is embedded in the matrix, the average axial stress

$\langle\sigma_f\rangle$ and the interfacial shear stress τ are both functions of z as the load is transferred from the fiber to the matrix. Note that the constraint boundary conditions are not denoted in the figure, as the derivation is independent of the constraint. Cox developed a shear-lag based solution for an embedded fiber. The relationship between the derivative of the fiber axial stress with respect to location and the shear stress at a given location is given by

$$\frac{d\langle\sigma_f(z)\rangle}{dz} = \frac{-4\tau(z)}{d_f} \tag{6}$$

The brackets denote average values, and are left from the original notation by Cox for emphasis. This relation can be derived from the free body diagram of an increment of the fiber of length Δz as shown in figure 3. Cox then showed that the average axial stress in the fiber satisfies the differential equation

$$\frac{\partial^2\langle\sigma_f(z)\rangle}{\partial z^2} - \beta^2\langle\sigma_f(z)\rangle = -\beta^2\langle\sigma_{f\infty}\rangle \tag{7}$$

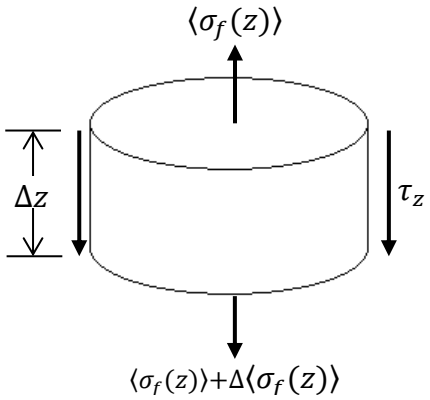

Figure 3. Free body diagram of an increment of fiber embedded in a matrix

where $\langle\sigma_f(z)\rangle$ is the average axial stress in the fiber as a function of z, β is the shear lag parameter, and $\langle\sigma_{f\infty}\rangle$ is the average axial stress at large z of a corresponding infinitely

long embedded fiber. For the macrobond test described in Figure 2b, the far field axial stress in the fiber is zero.

The shear lag parameter β originally proposed by Cox can be solved for using the equation

$$\beta = \frac{1}{\mathrm{r_f}}\sqrt{\frac{2\mathrm{G_m}}{\mathrm{E_f}\ln\frac{\mathrm{S}}{\mathrm{r_f}}}} \tag{8}$$

where G_m is the matrix shear modulus, E_f is the fiber axial modulus, r_f is the fiber radius, and S is the mean center-to-center separation of fibers normal to their length. The solution for β was then revised by Nayfeh to be

$$\beta = \left[\frac{2}{\left(\frac{d_f}{2}\right)^2 E_f E_m}\left(\frac{E_f V_f + E_m V_m}{\frac{V_m}{4G_f}+\frac{1}{2G_m}\left(\frac{1}{V_m}\ln\frac{1}{V_f}-1-\frac{V_f}{2}\right)}\right)\right]^{1/2} \tag{9}$$

where E_f, E_m, G_f, are G_m, are the Young's and shear moduli of the fiber and matrix respectively [22]. The radius of the fiber is $\frac{d_f}{2}$, the radius of the matrix is $\frac{d_m}{2}$, and both V_f and V_m are volumetric fractions defined as

$$\mathrm{V}_f = \left(\frac{d_f}{d_m}\right)^2 \tag{10}$$

and

$$\mathrm{V}_m = 1 - V_f \tag{11}$$

This solution of β has been widely used in place of Cox's expression [16]. We can begin to normalize equation 9 by rewriting it as

$$\beta = \frac{2}{d_f}\left[\frac{2}{E_f E_m}\left(\frac{E_f V_f + E_m V_m}{\frac{V_m}{4G_f}+\frac{1}{2G_m}\left(\frac{1}{V_m}ln\frac{1}{V_f}-1-\frac{V_f}{2}\right)}\right)\right]^{1/2} \tag{12}$$

The bracketed term in equation 12 is defined as C, resulting in

$$\beta = \frac{2C}{d_f} \tag{13}$$

Despite the form of the equation, from a physical standpoint the load transfer must be relatively independent of V_f, and V_m when $d_m >> d_f$. The concept of an effective matrix diameter, the size at which additional matrix material does not affect load transfer, has been used to account for this discrepancy. Considering this allows *C* to be considered a function of elastic moduli only when $d_m >> d_f$. For the axisymmetric macrobond, $\langle \sigma_{f\infty} \rangle$ is zero allowing the solution to equation 7 to be described by the characteristic equation

$$\langle \sigma_f(z) \rangle = C_1 e^{\beta Z} + C_2 e^{-\beta Z} \tag{14}$$

The boundary conditions that determine the values for C_1 and C_2 are the average axial stress at the locations z=0 and z=l_e, where l_e is the embedment length of the fiber. Applying the first boundary condition at z=0 yields

$$\langle \sigma_f(0) \rangle = C_1 + C_2 = \langle \sigma_0 \rangle \tag{15}$$

where $\langle \sigma_0 \rangle$ is the average stress acting on the free portion of the fiber (*i.e.* the applied load). We can then solve for C_2 in terms of C_1 and the stress $\langle \sigma_0 \rangle$

$$C_2 = \langle \sigma_0 \rangle - C_1 \tag{16}$$

The equation for the second boundary condition then becomes

$$\langle \sigma_f(l_e) \rangle = C_1 e^{\beta l_e} + (\langle \sigma_0 \rangle - C_1) e^{-\beta l_e} = 0 \tag{17}$$

C_1 becomes

$$C_1 = \frac{-\langle \sigma_0 \rangle e^{-\beta l_e}}{e^{\beta l_e} - e^{-\beta l_e}} \tag{18}$$

which simplifies to

$$C_1 = \frac{-\langle \sigma_0 \rangle}{e^{2\beta l_e} - 1} \tag{19}$$

We can now write the average stress equation in terms of the shear lag parameter β, initial stress $\langle\sigma_0\rangle$, and embedment length, l_e.

$$\langle\sigma_f(z)\rangle = \frac{\langle\sigma_0\rangle}{1-e^{-2\beta l_e}} e^{-\beta Z} - \frac{\langle\sigma_0\rangle}{e^{2\beta l_e-1}} e^{\beta Z} \tag{20}$$

We then apply equation 6, Cox's axial/shear stress relation to allow us to solve for the shear stress as a function of z

$$\tau_f(z) = \frac{d_f}{4}\left[\frac{\beta\langle\sigma_0\rangle}{1-e^{-2\beta l_e}} e^{-\beta Z} + \frac{\beta\langle\sigma_0\rangle}{e^{2\beta l_e-1}} e^{\beta Z}\right] \tag{21}$$

Equations 20 and 21 can be adapted to the first case of infinite embedment length by taking the limit $l_e \to \infty$. These equations then take the form

$$\lim_{l_e\to\infty} \langle\sigma_f(z)\rangle = \langle\sigma_0\rangle e^{-\beta Z} \tag{22}$$

$$\lim_{l_e\to\infty} \tau_f(z) = \frac{d_f}{4}\left[\beta\langle\sigma_0\rangle e^{-\beta Z}\right] \tag{23}$$

Fully Embedded Single Fiber

This approach can be extended to the case of a fiber that is fully embedded in a matrix material, as shown in figure 2c. In this case, the full fiber length spans from 0 to $2l_e$, but we consider only half of the fiber so that z can range from 0 to l_e, with z=0 at the free end of the fiber and z=l_e at the midplane of the fiber. The stress at z=l_e is equal to $\langle\sigma_\infty\rangle$ for large values of l_e, and can be calculated by using the rule of mixtures for composites [34]. As the fiber stresses no longer approach zero for large z, the characteristic equation derived from equation 7 becomes

$$C_1 e^{\beta Z} + C_2 e^{-\beta Z} = -\beta^2\langle\sigma_{f\infty}\rangle \tag{24}$$

where $\langle\sigma_{f\infty}\rangle$ describes the far field stress as some constant denoted as $\langle\sigma_\infty\rangle$, which is equal to the stress in the fiber at large z. The solution to this equation then takes the form

$$\langle\sigma_f(z)\rangle = C_1 e^{\beta Z} + C_2 e^{-\beta Z} + \langle\sigma_\infty\rangle \tag{25}$$

The rule of mixtures [34] states that for long fibers, a longitudinally loaded composite is treated as two springs in parallel and therefore both fiber and matrix materials have equal strain. The effective Young's modulus is given by a combination of fiber and matrix moduli weighted by their volumetric fractions given by equations 10 and 11. The upper bound strain in the composite and the composite's Young's modulus for a longitudinally loaded fiber are written as

$$\varepsilon_C = \varepsilon_f = \varepsilon_m \tag{26}$$

$$E_c = \left(V_f E_f\right) + (V_m E_m) \tag{27}$$

where ε_c is the strain in the overall composite, ε_f is the strain in the fiber, ε_m is the strain in the matrix material, and E_c is the effective modulus of the composite. Once the effective Young's moduli are calculated, the effective stresses can found by the use of Hooke's law.

$$\langle\sigma_c\rangle = \left(V_f\langle\sigma_\infty\rangle\right) + (V_m\langle\sigma_m\rangle) \tag{28}$$

$$\langle\sigma_\infty\rangle = \frac{(E_c\varepsilon_C)-(V_m\varepsilon_C E_m)}{V_f} \tag{29}$$

The artificial boundary conditions for the problem are that the stress at the free end of the fiber is zero, expressed as

$$\langle\sigma_0\rangle = 0 \tag{30}$$

and that symmetry conditions exist in the middle of the fiber, expressed as

$$\frac{\partial\sigma_{l_e}}{\partial z} = 0 \tag{31}$$

Considering the first boundary condition leads to

$$C_1 + C_2 = -\langle\sigma_\infty\rangle \tag{32}$$

Solving for C_1 first and substituting into equation 25 allows us to solve for C_2 which becomes

$$C_2 = \frac{-\langle\sigma_\infty\rangle}{1+e^{2\beta l_e}} \tag{33}$$

Substituting equation 33 into 32 allows us to find C_1 which becomes

$$C_1 = \frac{-\langle\sigma_\infty\rangle}{1+e^{-2\beta l_e}} \tag{34}$$

Equation 25 then takes the form

$$\langle\sigma_f(z)\rangle = \frac{-\langle\sigma_\infty\rangle}{1+e^{-2\beta l_e}}e^{\beta Z} - \frac{\langle\sigma_\infty\rangle}{1+e^{2\beta l_e}}e^{-\beta Z} + \langle\sigma_\infty\rangle \tag{35}$$

We can then obtain the shear stress as a function of z by using Cox's relation in equation 6.

$$\tau_f(z) = \frac{-d_f}{4}\left[\frac{\beta\sigma_\infty}{1+e^{2\beta l_e}}e^{-\beta Z} - \frac{\beta\sigma_\infty}{1+e^{-2\beta l_e}}e^{\beta Z}\right] \tag{36}$$

Note that the main difference between these two configurations is that for a single exposed fiber the initial stress acting on the free end of the fiber must be known for the analysis whereas the configuration of a fully embedded fiber requires the far field midplane stress of the fiber determined from the law of mixtures.

Chapter 5

Finite Element Analyses

Infinite Embedment Length Case

All finite element models discussed in this thesis were created and analyzed with Comsol Multiphysics software with each geometry composed of axisymmetric elements. The first case studied was intended to represent an infinite embedment length. Single fiber pull out and macrobond boundary conditions were used in the analysis and can be seen in figure 4. The boundary conditions used to create each geometry were simulated by using roller constraints in the appropriate locations. The matrix diameter was $40d_f$ and the embedment length was $20d_f$ for preliminary analyses to approximate the case of infinite embedment length. Sensitivity studies suggest that these matrix dimensions are large compared to the fiber radius and the resulting normalized solutions presented in this paper are not sensitive to small changes in the dimensions.

The boundary conditions for the fiber pull out study included the bottom of the composite (fiber and matrix) fixed against translation in the *z* direction through the use of the aforementioned roller constraint. The modeling program automatically assigned boundaries to fix the axis of symmetry against translation in the *r* direction.

The geometry for the macrobond tests was kept the same, but the boundary conditions were changed. For this configuration, the roller constraint was moved from the bottom of the composite to the top of the matrix material only. A convergence study was used to determine the distance from the fiber interface to the roller constraint. This distance was to be the appropriate size for the hole in the macrobond testing apparatus

used by Holsman *et al* [26]. The hole was expanded until the measured value of average axial stress $\langle \sigma_f \rangle$ at the beginning of the fiber/matrix interface approached the initial stress acting on the free end of the fiber $\langle \sigma_0 \rangle$. The diameter for the hole was evaluated to be approximately two fiber diameters. The combination of a long embedment length and a large hole diameter was sought for the purposes of decreasing stress concentrations in the system.

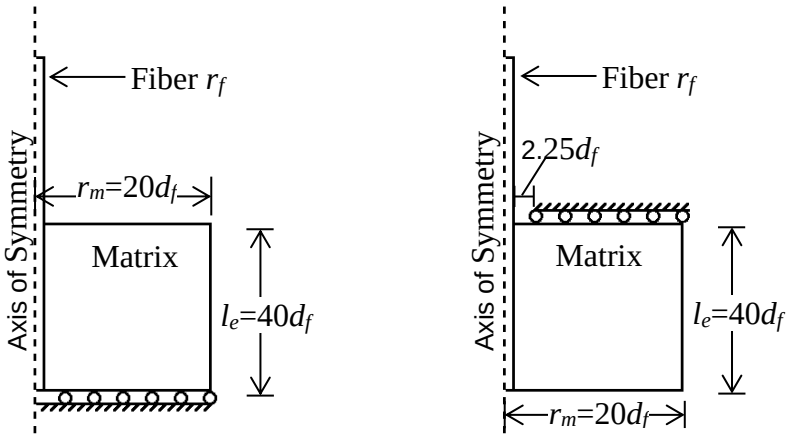

Figure 4. Axisymmetric configurations representing a) pullout, and b) axisymmetric macrobond test

A range of λ of 0.33 to 80 were used to study these configurations.

Quadratic quadrilateral and triangular shaped elements were used to model the composite. A uniform quadrilateral mesh was generated within the fiber, while triangular elements were used within the matrix. A close up view of the fiber/matrix interface region is shown in figure 5. A convergence study was conducted to find the appropriate element size for the fiber, growth ratio for the triangular elements in the matrix, and the maximum element size for the matrix. The symmetric quadrilateral elements used within the fiber were made to have a length of 0.02d_f. The triangular elements used in the

matrix started at the fiber/matrix interface with the same element length as the square mesh and grew at a rate of 20 percent of the adjacent element.

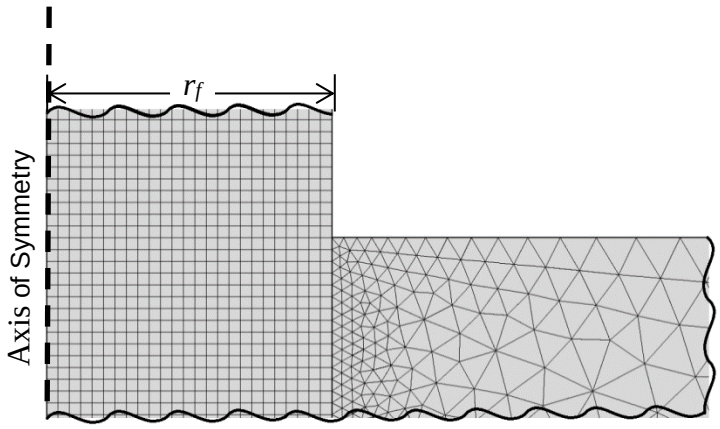

Figure 5. Optimized mesh for FEA analyses

Finite Embedment Length Case

The macrobond geometry and boundary conditions were used exclusively to analyze the case of finite embedment length. The geometry was modified to closely resemble experiments performed by Holsman, *et al.* [26] so that a better comparison between the numerical model and their experimental results could be obtained. Modifications included reducing the fiber diameter to 0.0105in (30 Gauge) and reducing the embedment length to less than $10d_f$. The matrix material was also repositioned to be approximately $95d_f$ (1in) above the fiber end to better simulate experiments by Holsman *et al*. It should be noted that sensitivity studies showed that repositioning the matrix material away from the fiber end (*i.e.* bottom fixity BC) had no effect on load transfer. The geometry used for finite embedment length studies can be seen in figure 6. The most extreme case considered in the analyses consisted of an embedment length of $3d_f$ and a

hole diameter of 1.1d_f. This analysis was then performed for values of λ ranging from 1 to 80. Studies of the effects of hole diameter started with a diameter of 1.1d_f which represents a hole size that is reasonably similar to that used for experiments described by Holsman *et al*. and ending with a diameter of 3d_f. Results from FEA simulations exhibited behavior similar to that reported by Herrera-Franco [35]. γ values ranging from 3 to 30 were also evaluated for each hole diameter.

Results were extracted in the form of stress vs location for shear stress taken along the fiber/matrix interface. Average axial stress was taken from calculating the average stress along a 2D cross-sectional cutlines placed along the fiber radius. Cutlines were taken at intervals of 0.10d_f along the *z* axis fibers with a length of less than 10d_f and intervals of 0.25d_f for fibers with a length over 10d_f.

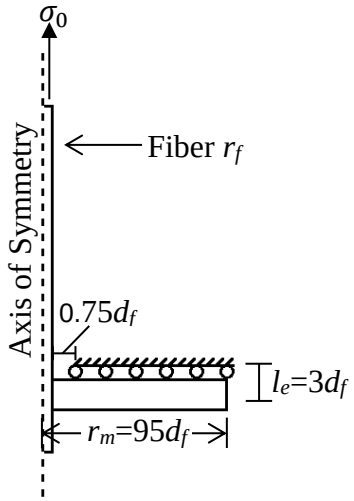

Figure 6. Geometry for macrobond tests with finite embedment lengths

Fully Embedded Fiber Case

The final case of a fully embedded fiber was modeled with axisymmetric concentric circles. The fiber diameter from the second case of a finite macrobond geometry was kept for the fully embedded geometry. The fiber was then centered in a matrix consisting of a constant length of 5in and a radius of $10d_f$ while 6 fiber lengths starting from $3d_f$ and ending at $100d_f$ were studied. λ of the composite was kept constant at a value of 40 for all studies. A roller constraint was placed on the bottom edge of the matrix to enforce boundary conditions while a specified load was placed on the top edge of the matrix. The same elements and element sizes from the single exposed fiber configurations were used for this configuration. Again, symmetric square elements of $0.02d_f$ were placed inside the fiber and triangular elements with a growth rate of 20% were placed in the matrix. The geometry with its dimensions and boundary conditions can be seen in figure 7

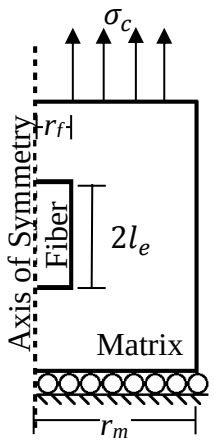

Figure 7. Geometry for fragmentation test

For these analyses, it was assumed the solution was symmetric about the midplane and therefore, only fiber stresses from half of the fiber were used for the comparison to the analytical solution. Numerical solutions for shear stress were obtained from the lower half of the fiber/matrix interface. In addition to the use of cross-sectional cutlines to pull solutions for average axial stress, the non-averaged axial stress along the axis of radial symmetry was pulled from the analyses. At a given distance z from the end of the fiber, the average axial stress on the cross section of the fiber disagrees with non-averaged axial stress along the axis of symmetry for a distance of approximately 1 fiber diameter. At 1 fiber diameter from the free surface, the difference between these two values is less than 2%, and continues to decrease to well below 1% by 2 fiber diameters. This study was conducted for fiber lengths of $3d_f$, $5d_f$, and $10d_f$.

Chapter 6

Comparison between FEA and Shear Lag Theory

The shear lag parameter β is sensitive to the geometry of the pull-out scenario. For this reason it is not widely used for characterizing interfacial bond strength. Zhandarov *et al.* [24] proposed using β as a fitting parameter to experimentally fit β using average debond stress. Holsman *et al.* [26] expanded on this method by using a normalized β value denoted as C to fit debond stress through multiple fiber diameters.

In this study β was also used as a fitting parameter to minimize the error between the analytical and FEA solutions for shear and average axial stress. This best fit method to determine β in this thesis is similar to that used by Galiotis [13] but is different from that used by Zhandarov *et al*. [24] and Holsman *et al*. [26]. Galiotis *et al*. found the value of β that resulted in a least squares error between axial fiber stress found from experimentally measured strains and fiber stress predicted with a shear lag model. In this thesis, fiber stress found using finite element analyses are used instead of experimentally measured values. In the studies by Zhandarov *et al*. and Holsman *et al*., the failure loads from multiple tests were plotted against embedment length or normalized embedment length, and both ultimate interfacial shear strength and β or C were varied until a best fit with the experimental data was obtained.

In this approach, the value of β is varied until the analytical solution in question agrees with the corresponding FEA solution for a given value of z. Several methods can be applied by choosing which type of stress to compare. Initially, the shear lag and FEA solutions were compared by using average axial stress by embedded the solutions in the

equation for strain energy per unit volume. This method squares the values of average axial stress for a given value of *z* achieving a more critical fitting of β. Solutions from the FEA are not dimensionless or normalized so the shear lag parameter β must be used in the least squares fit and then made dimensionless after being optimized. This method takes the form

$$f_\beta = \pi r_f^2 \Delta z \sum_{z_i=0}^{l_e} \left[\left(\frac{\langle \sigma_{SL_i} \rangle^2}{2E_f} - \frac{\langle \sigma_{FEA_i} \rangle^2}{2E_f} \right) \right]^2 \tag{37}$$

where $\langle \sigma_{SL_i} \rangle$ is the shear lag solution from equation 20 for a given value of z, $\langle \sigma_{FEA_i} \rangle$ is the corresponding solution from the FEA, Δz is the difference between z_{i+1} and z_i, r_f is the radius of the fiber, and E_f is the Young's modulus of the fiber. Once a value of β that results in a minimum error was found, equation 13 was used to solve for a corresponding *C* value for use in further studies. The least squares fit was evaluated using thirty different values of β. The domain was adjusted until a minimum value was located and then reduced to increase resolution. A typical error distribution from this method can be seen in figure 8.

Initial difficulties in obtaining a sufficient number of values of strain energy per unit volume for the required detail of fit led to a second method of least squares optimization in which the shear stress solutions were directly compared. This method takes the form

$$f_\beta = \sum_{z_i=0}^{l_e} \left[\left(\tau_{SL_i} - \tau_{FEA_i} \right) \right]^2 \tag{38}$$

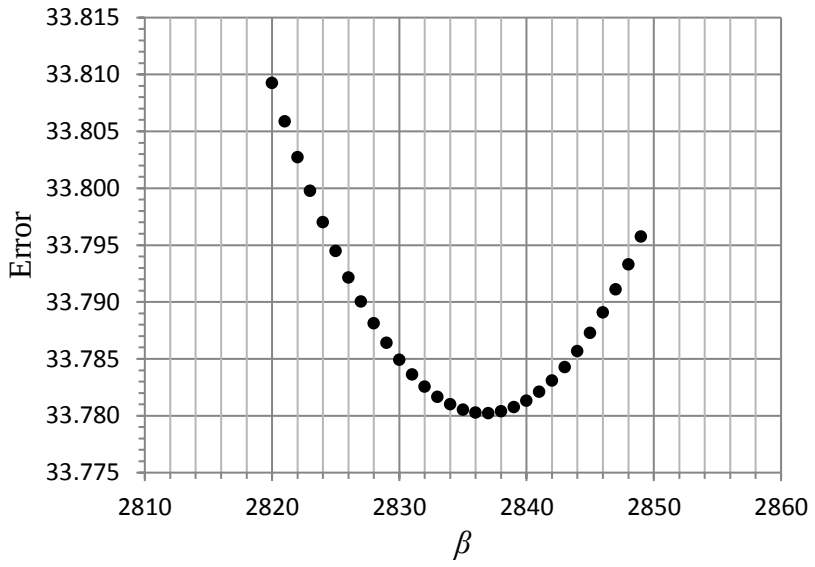

Figure 8. Minimized error function for γ=10, λ=10, α=1.5

where τ_{SL_i} is the shear lag solution from equation 21 for a specified value of z and τ_{FEA_i} is the corresponding FEA solution. Using this method allowed for both a large increase in the number of values used in the fit and a reduction of Δz. To evaluate the case of a fully embedded fiber, the method described by equations 38 was altered by using the shear lag solution described by equation 36.

After optimizing β by use of equation 38, the shear lag solutions were plotted against the FEA solutions for both shear and average axial stress and can be seen in figures 9 and 10. Solutions for SL and FEA were normalized by diving all solutions by the initial axial stress acting on the fiber.

Fitting methods using equations 37 and 38 were compared while simultaneously comparing the difference in boundary conditions for an infinitely embedded exposed single fiber. The resulting strain energy-optimized values of *C*, along with shear-stress-optimized values of *C* are plotted against λ in figure 11 for both pull-out and axisymmetric macrobond configurations.

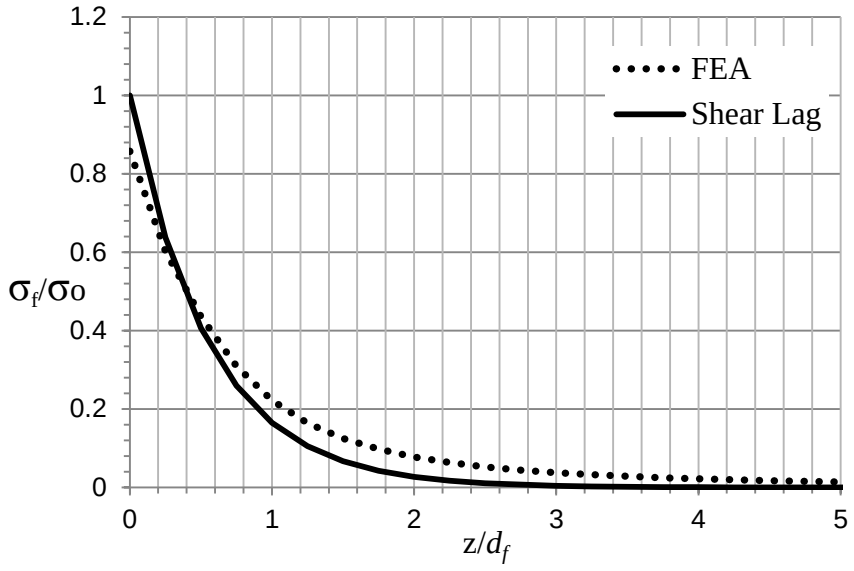

Figure 9. Normalized values of SL average stress and FEA average stress located along the embedded fiber length

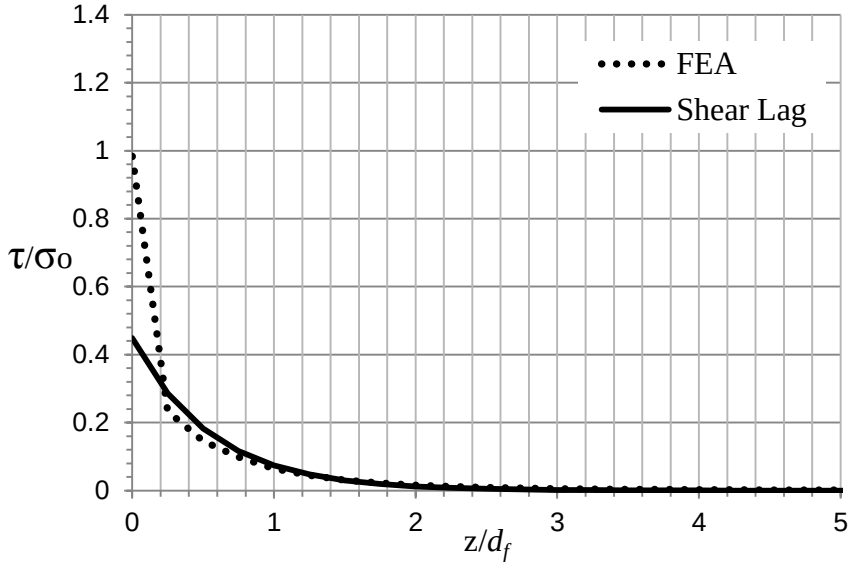

Figure 10. Normalized values of SL shear stress and FEA shear stress located along the embedded fiber length

When shear stress was used to optimize β at low values of λ, the calculated values of C were higher than the values calculated by using average axial stress for the optimization. For λ=0.33, a difference in C of 0.224 was observed. However, this difference had an inverse relationship with λ. For λ=10, a difference of only 0.0224 was observed. An apparently erroneous result was observed for the strain energy-optimized pull-out data for λ=2. It was determined that the limited number of z values used for the least squares fit did not provide enough resolution to capture the full behavior of the model. It is anticipated that increasing the number of z values for which data are obtained would result in this data point approaching the trend for the other data. A more detailed comparison between the top and bottom fixity boundary conditions and between shear and strain energy optimization of β was performed by Avery *et al*. [36].

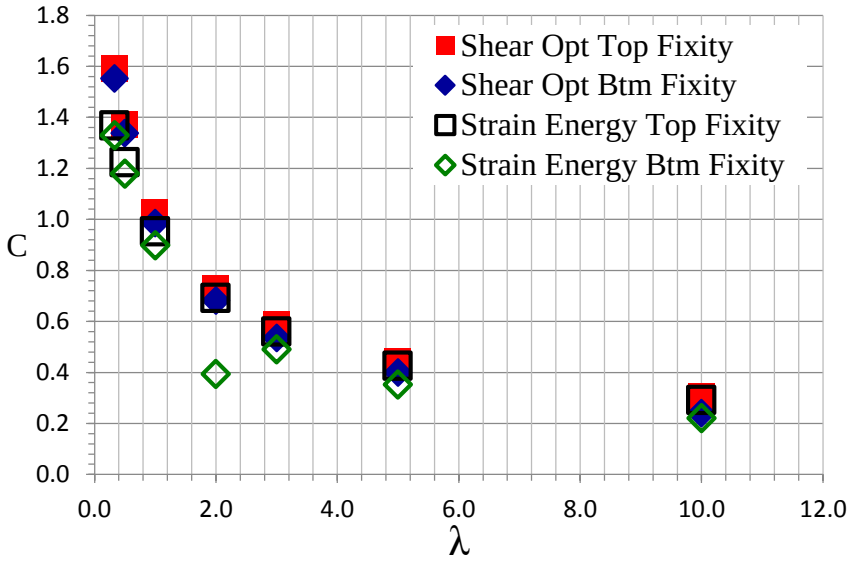

Figure 11. Optimized C fit vs. λ

The lack of resolution in the behavior of average axial stress needed to be addressed so that a more detailed behavior of the configurations being modeled could be observed. The nature of the FEA software was that the number of data points for shear stress pulled from the fiber/matrix interface was two orders of magnitude greater than the number of cross-sectional cutline data points obtained within an acceptable time limit. The average axial stress values for a given z were needed for the comparison of strain energy per unit volume, therefore it was decided that equation 38 would be used to fit β for the remaining analyses along with using Cox's relation from equation 6 to integrate the FEA shear stress solution and create a quasi FEA solution for average axial stress. The values for average axial stress would ultimately be a shear lag solution but obtained from FEA values. The result was good agreement between the FEA and shear lag solutions for average axial stress among most specimen geometries modeled. Validation of this new method was shown when the new method converged with average axial stress values taken from cross-sectional cutlines along the fiber length. This also allowed insight into whether it was better to optimize β using shear stress or average axial stress.

Throughout the study, specific parameters of the configuration were varied so that the effects of these parameters could be observed. This allowed for a diverse degree of agreements between the shear lag and FEA solutions for shear stress. Even though the agreement of the two solutions for shear stress ranged from poor to good, the agreement between the two solutions for average axial stress never extensively deteriorated.

When fully embedded fibers were studied, the method of integrating shear became insufficient to study the behavior of average axial stress. For long fiber lengths, the average axial stress derived from equation 6 fell short of the analytical solution for

maximum fiber stress. Non-averaged axial stress values were pulled from the axis of symmetry along the fiber portion of the composite for the new series of comparisons. The new series of axial stress values were compared to average values taken from cutline's places every 0.10 fiber diameters. Fiber lengths of $3d_f$, $5d_f$, and $10d_f$ were used for validation purposes. For each case, at a given z value greater than one fiber diameter away from the free end, the average axial stress over the entire cross section agrees with the axial stress along the axis, *i.e.* at r=0.0. The new values of axial stress allowed for the FEA and shear lag solutions optimized by equation 38 to converge, but for long fiber lengths of $50d_f$ and longer. The non-averaged axial stress values were used directly in a least squares fit to optimize β in the same way that the shear stress values were used.

$$f_\beta = \sum_{z_i=0}^{l_e}\left[\left(\sigma_{SL_i} - \sigma_{FEA_i}\right)\right]^2 \tag{39}$$

This new method allowed for a convergence in midplane axial stress values for all fiber lengths with only slight variations in the agreement between solutions. Axial stress was then used to optimize β for all cases of the fully embedded fiber.

Chapter 7

Effects of Geometric and Material Parameters

The pull out and macrobond configurations were evaluated for long embedment lengths and constant hole size for the macrobond configuration such that only λ was varied. The long embedment length ensured that the axial stress in the fiber behaved as the infinite embedment length case would. For the macrobond configuration, the hole size was chosen to be in a range where the effect on changes in hole size would have a small effect on the fitted value of *C*. As λ increased, the rate of stress transfer decreased and consequently so does the fitted value of *C*. This behavior can be observed in figure 12.

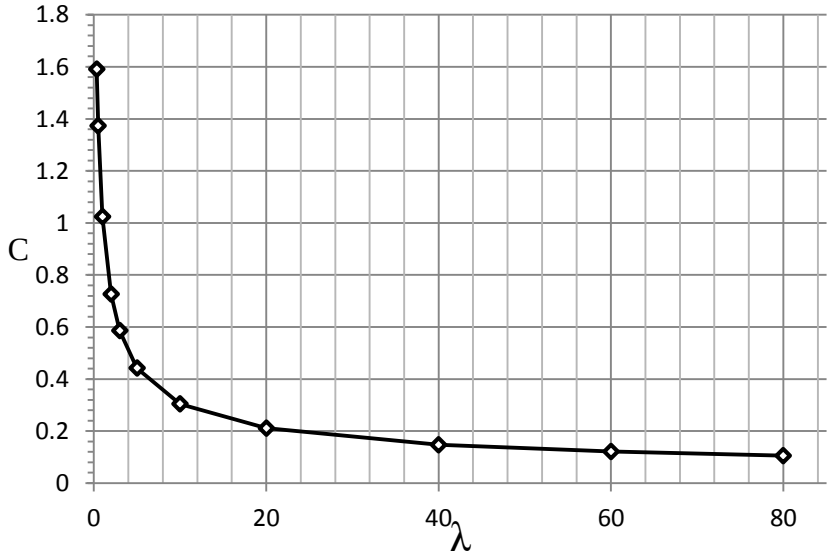

Figure 12. λ effects on the infinite macrobond geometry

The macrobond test configuration with a top fixity boundary condition was considered to study the effects of changes in γ and α on the fitted value of *C*. In addition to varying γ and α, a range of λ was also varied so that better insight could be obtained toward the creation of a macrobond test. The most extreme case for embedment length of $3d_f$ was used for the initial study. The hole diameter of the macrobond configuration was set to a mean value of $1.5d_f$. Figure 13 shows the shear stress along the fiber-matrix interface as a function of the location along the z axis for both FEA and the best fit shear lag solution. Figure 14 shows the average axial stress comparison using data collected from cross-sectional cutlines every placed every $0.10d_f$ and the best fit shear lag solution.

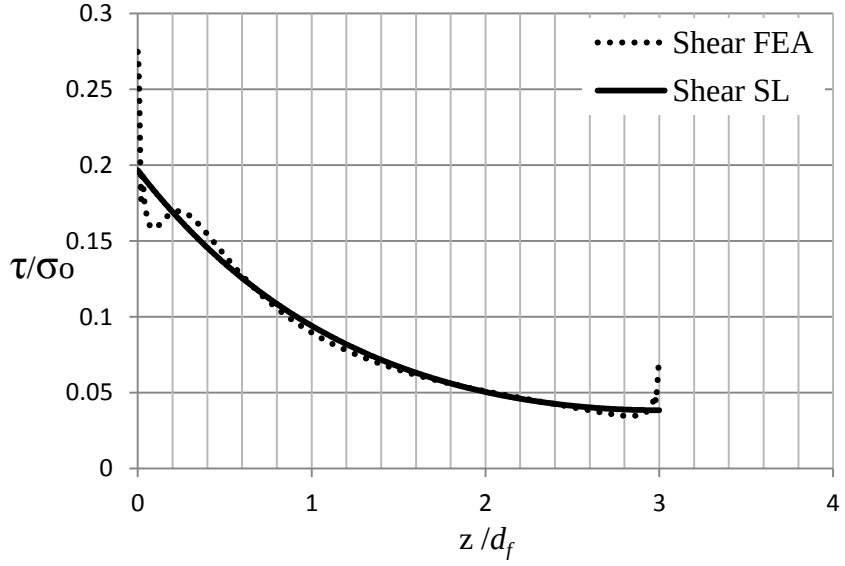

Figure 13. FEA and SL solutions for shear stress plotted against location along the z axis for λ=15.625, γ= 3, α=1.5

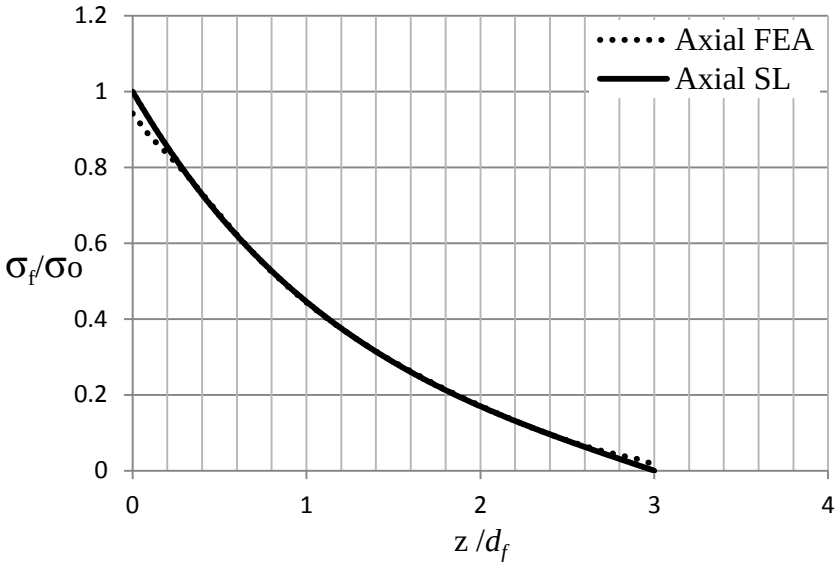

Figure 14. FEA and SL solutions for average axial stress plotted against location along the z axis for λ=15.625, γ= 3, α=1.5

When the shear lag solution was plotted against the FEA solution for the stress transfer behavior along the fiber-matrix interface, the shear lag solution was in good agreement except near the matrix surfaces. A singularity exists at the point of z=0 where the stresses approach infinity [16,23]. At the end of the fiber there is also a sharp increase in shear where the load being transferred from the fiber is not allowed to approach zero. It is at these points that the shear lag solution does not capture the true behavior of the composite.

Effects of Hole Diameter α and Embedment Length γ on *β*

An oscillation in the stress curve of the numerical solution for shear occurs for geometries with a finite embedment length. A sensitivity study on the effect of the hole diameter on the oscillation was conducted using values of α ranging from 1.1 to 3 seen in figure 15.

The magnitude of stress concentrations near the matrix surface increases as the hole diameter approaches the diameter of the fiber. As the size of the hole increases the amplitude of the oscillation decreased and the oscillation itself shifted away from the beginning of the fiber/matrix interface. The presence of this initial spike in shear stress increased the fitted value of C up to 2.5 times the value for an infinite case when using a hole diameter of $1.1d_f$. This correlation was further studied by plotting each fitted value of C against α in figure 16. The impact of the hole diameter on the effective value of C began to decrease after a value of $1.6d_f$, but the value of C never truly converged within a reasonable range of hole diameters.

To further analyze the effects of the hole diameter on the value of the fitted C, a parametric sweep of hole diameters was extended to different values of λ. C values were fitted from configurations with λ values ranging from 1 to 80 and α values ranging 1.1 to 3 while γ was kept at a constant value of 5. A constant embedment length of $5d_f$ was chosen to represent a regime between highly finite and infinite behavior. These plots can be seen in figure 17.

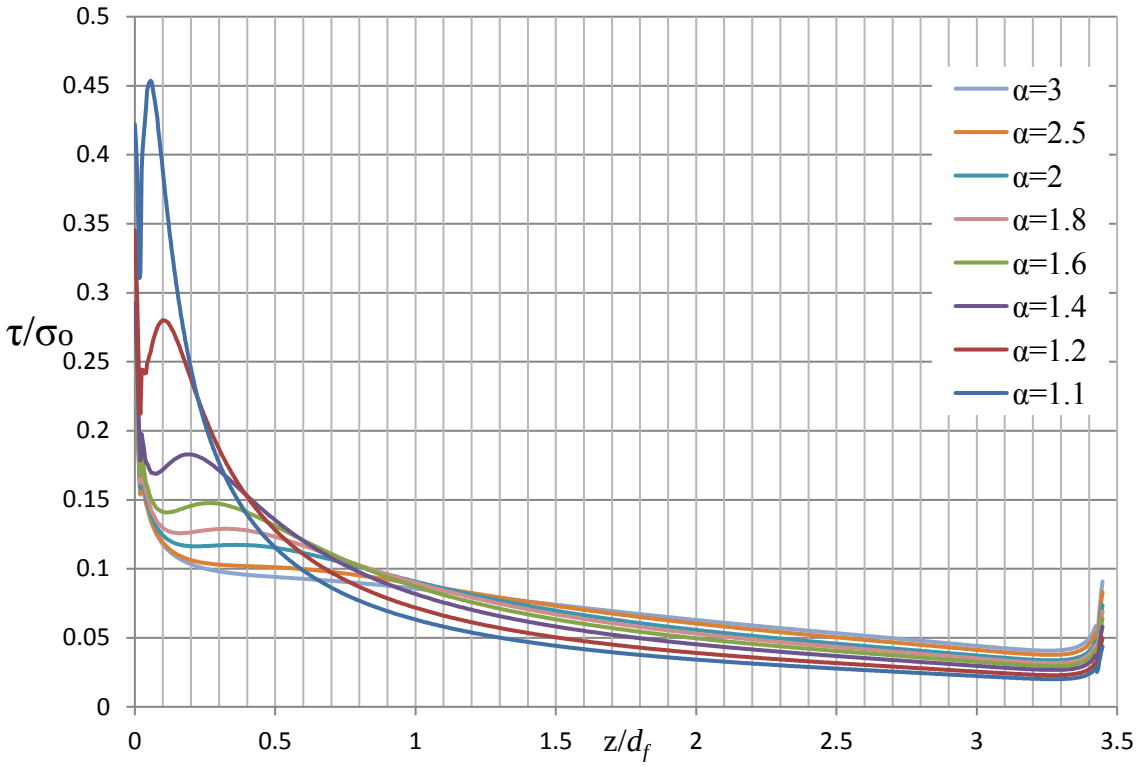

Figure 15. Interfacial shear stress plotted along fiber-matrix interface for various α values

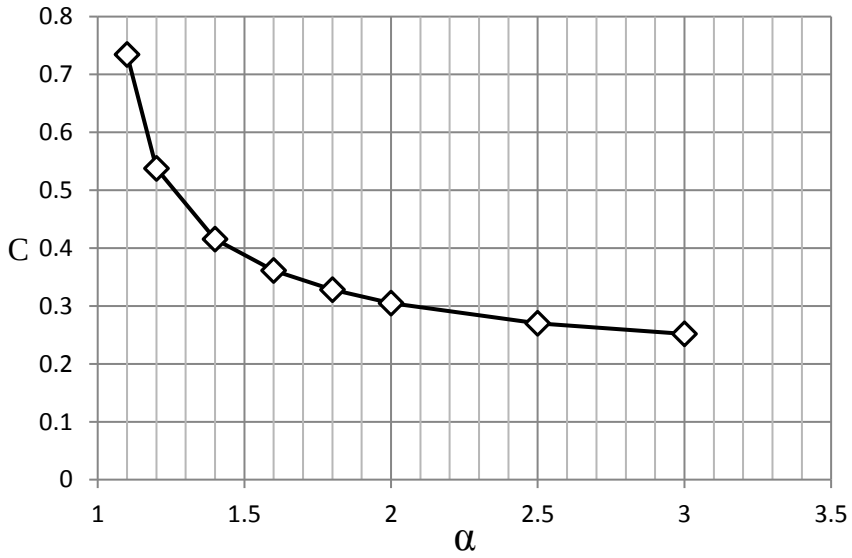

Figure 16. Best fit values of *C* plotted against hole diameter for γ=3, λ=15.625

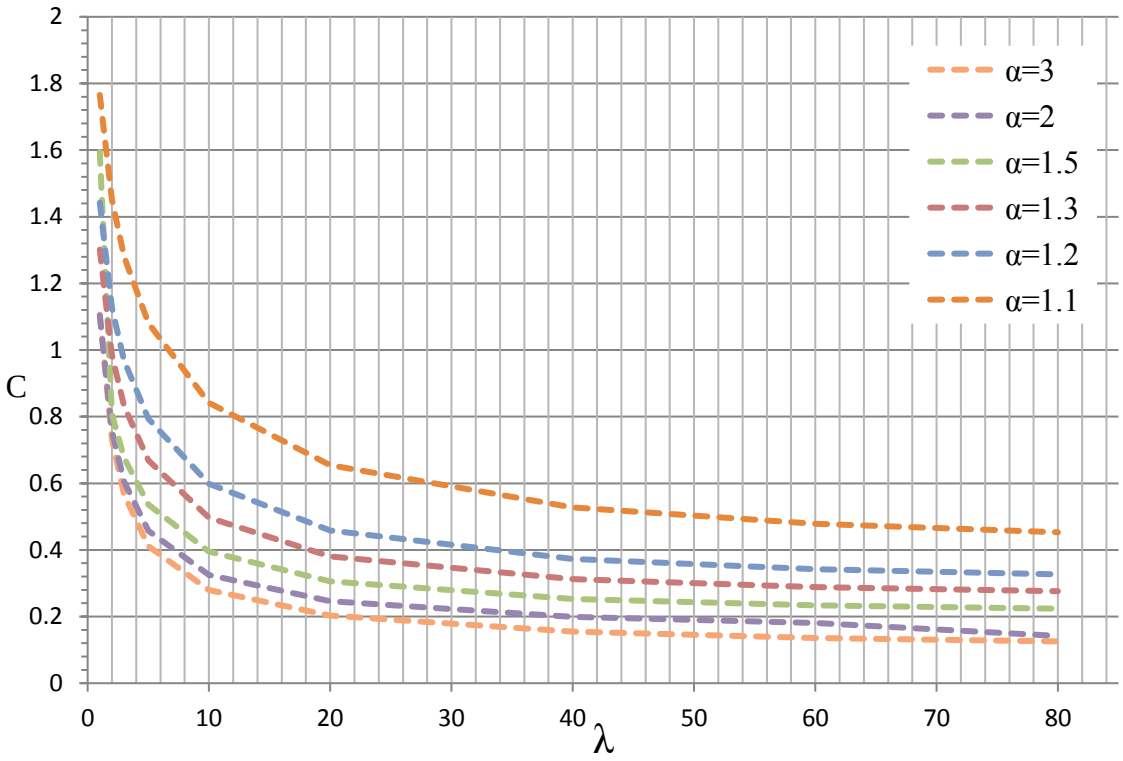

Figure 17. *C* vs λ for α=1.1-3, γ=5

The behavior of *C* as a function of λ stays consistent throughout the range of α. As the diameter of the hole is reduced the higher stress concentrations shift the plots of *C* vs λ higher while retaining the same behavior for each data series. As the hole diameter decreases the rise in the initial stress concentration allows more load to be transferred at low values of *z*. The resultant higher *C* values reflect a more rapid transfer of force from the fiber.

The same type of analysis was carried out to determine the effects of embedment length on the fitted value of *C*. The initial test geometry with α=1.5 and λ=15.625 was evaluated with different embedment lengths starting from the most extreme case of $3d_f$ to a depth of $30d_f$. The plots of shear vs normalized location along the fiber axis for each value of embedment length l_e can be seen in figure 18.

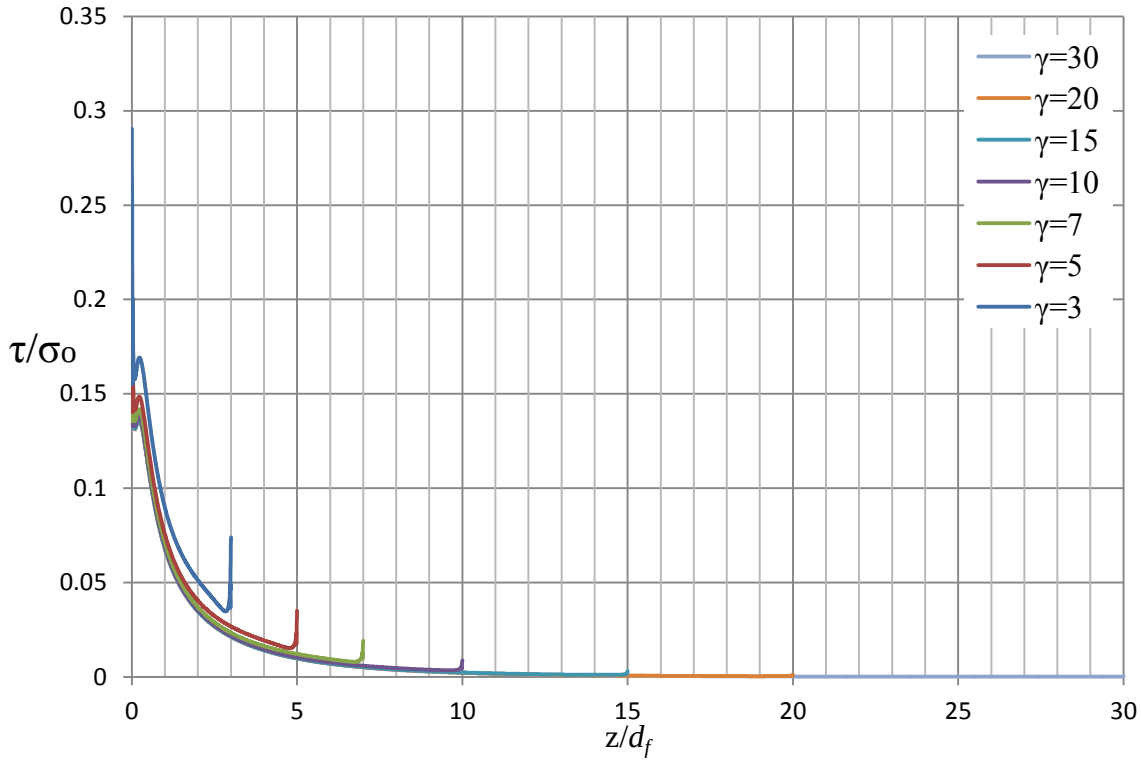

Figure 18. Embedment length effect on shear stress along fiber-matrix interface for α=1.5 and γ=15.625

There is a noticeable stress concentration at end of fibers with short embedment lengths. This stress concentration reduces in magnitude as the embedment length increases, and is not discernable for embedment lengths greater than 10 or 15 fiber diameters. An increase in the amplitude of the oscillation occurs at short embedment lengths. As the embedment length increase the amplitude decreased but did not translate across the fiber-matrix interface as it did when hole diameter was varied. Figure 19 shows values of *C* corresponding to each value of γ used.

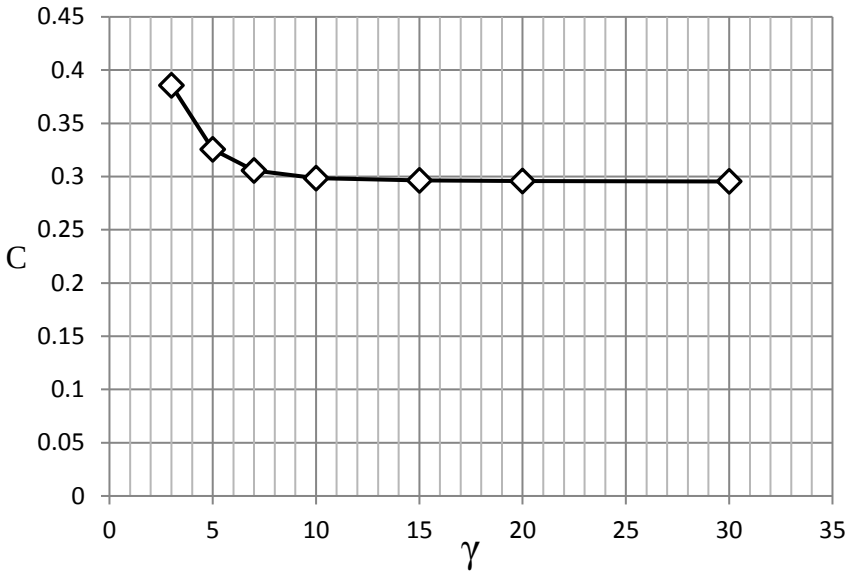

Figure 19. Embedment length effect on *C* as a function of γ

The fitted values of *C* converged for γ values greater than 10. This can be attributed to the fact that the constant C_1 from the shear lag solution in equation 20 for average axial stress approaches zero for large values of γ and take on the behavior described by equation 22. Therefore, configurations where $\gamma \geq 10$ can be considered to have an infinite embedment length and behave correspondingly.

The same range of λ was then evaluated for the values of embedment length used for the convergence study. The results can be seen in figure 20.

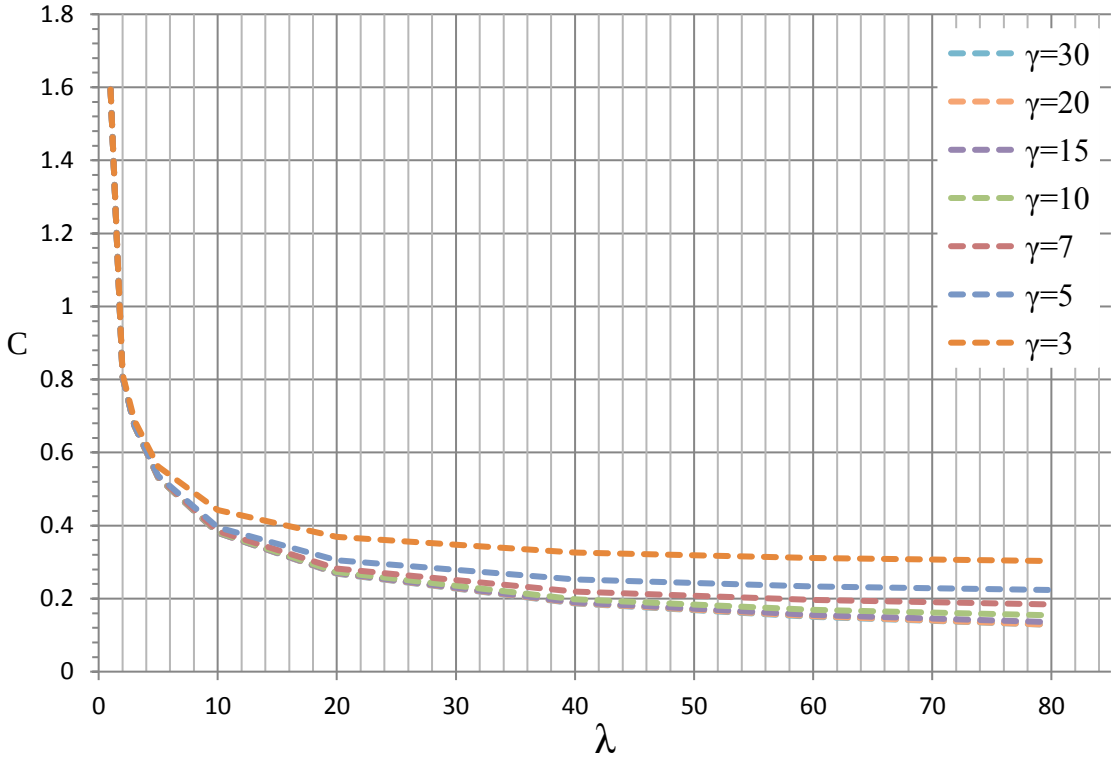

Figure 20. Effect of λ on *C* for γ=3-30, α=1.5

At values of λ less than 10, the fitted values of *C* converged to a single value. As the Young's modulus of the fiber increases, the stress concentration at the matrix surface *i.e. z*=0.0 increases. These stress concentrations are further increased for shorter embedment lengths. From figure 20 we can see that after γ=10 the fitted values of *C* become similar in magnitude for all values of λ and behave approximately the same for configurations with embedment lengths of 10, 15, 20, and 30 fiber diameters.

Results from these models were compared to identify parameter values that led to the highest values *C*. A correlation between *C* and the initial stress concentration at the beginning of the fiber/matrix interface allows for a simultaneous insight into which cases create the highest stress concentrations where the fiber meets the matrix. This combination of parameters was observed to have the lowest values of γ and α along with

the highest value of λ used from the previous studies. A model with these parameter values was then used to further test the accuracy of using shear stress to optimize *C*. The resulting shear lag solutions for shear and axial stress can be seen compared to their respective numerical solutions in figures 21 and 22 respectively. The shear stress comparison shows a poor fit, in which the shear lag solution misses most of the numerical behavior. However, the resultant solutions for average axial stress show much better agreement.

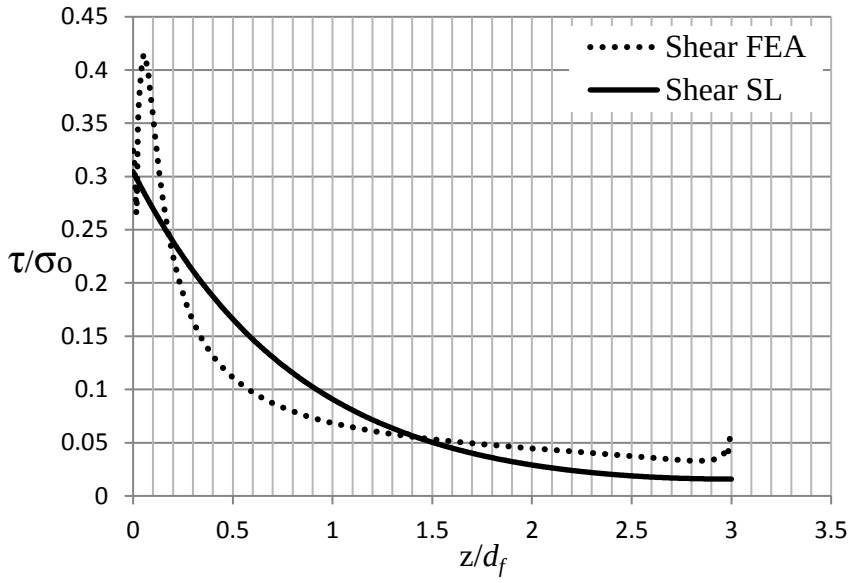

Figure 21. FEA vs SL for shear stress corresponding to γ=3, α=1.1, λ=100

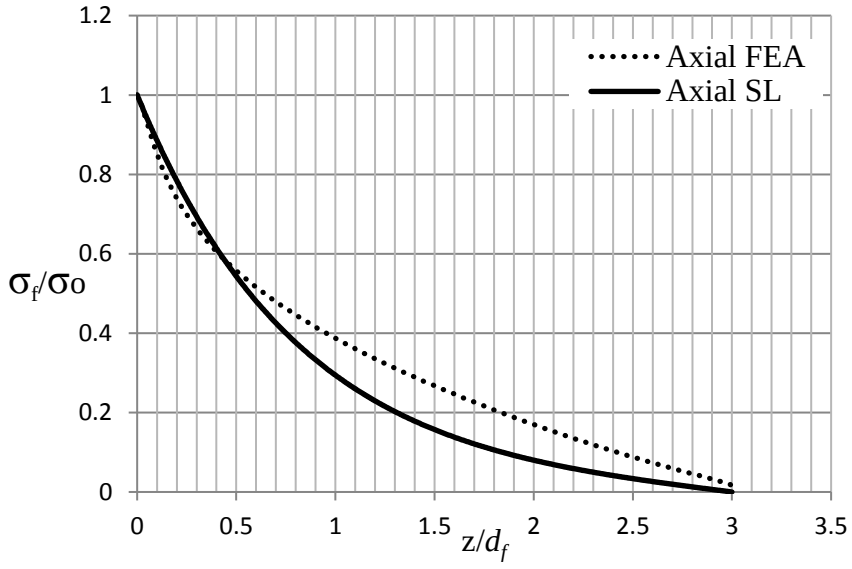

Figure 22. FEA vs SL for average axial stress corresponding to γ=3, α=1.1, λ=100

Fully Embedded Fiber Results

As there is no hole in the fully embedded fiber configuration, only the parameters λ, and γ remained for consideration. The effects of embedment length were analyzed by using a range of γ=3 to 100. For composites, a critical fiber length exists which governs the fiber's ability to carry its maximum load [34]. This solution for this limit takes the form

$$l_c = \frac{\sigma^*_f d_f}{2\tau_c} \tag{40}$$

where l_c is the is the critical length dependent on the fiber's ultimate tensile strength σ^*_f and diameter d_f in addition to the ultimate interfacial shear strength τ_c. If a fiber is shorter than the critical fiber length, only a partial amount of load from the matrix can be transferred. The maximum value of γ=100 was chosen to be above this critical length allowing the fiber to be treated as an idealized infinite fiber. This allows for the rule of mixtures to be used to calculate internal axial stresses and strains at fiber midlength. The

shear lag solutions for all values of γ were evaluated with the same value of σ_∞ calculated by equation 26. A behavior similar to the exposed fiber configuration was observed in the sense that the fitted value of *C* had an inverse relationship to the value of embedment length. A plot of *C* vs embedment length can be seen in figure 23. The fitted value of *C* starts to converge for embedment lengths of $25d_f$, even though the data point at γ=25 seems slightly out of place. It should be noted that this behavior was observed in the fully embedded, *i.e.*, fragmentation configuration when γ≥25 as opposed to γ≥10 for exposed fibers. The stress solutions for axial and shear stress for each fiber geometry can be seen in figures 24 and 25 respectively. Embedment lengths less than $50d_f$ do not reach the fiber stress value from equation 26. However, the final axial stress values from both solutions converged for every value of embedment length. The shear lag solutions for shear stress showed less agreement with corresponding FEA at short embedment lengths. The slope of the function took on a linear characteristic for embedment lengths less than 25 fiber diameters. Both shear lag and FEA solutions converged at $z=l_e$.

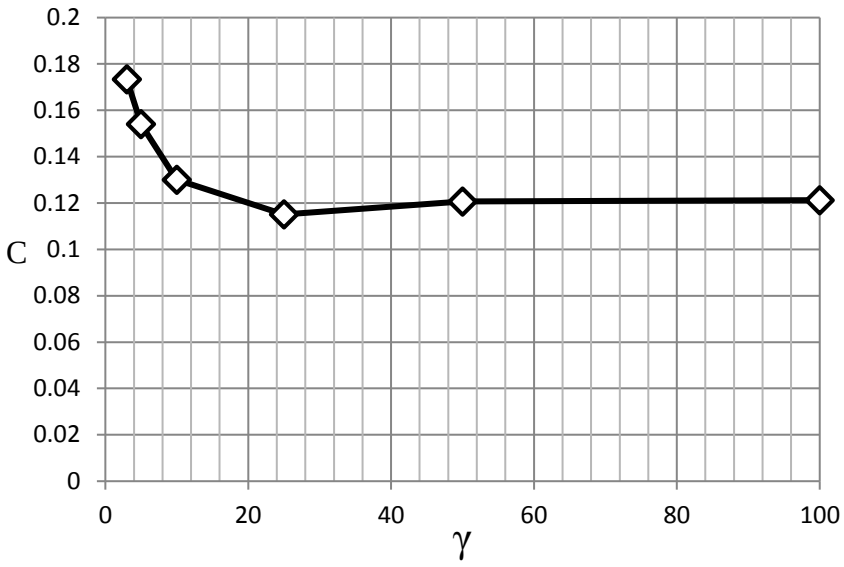

Figure 23. Embedment length effect on *C* for a fully embedded fiber

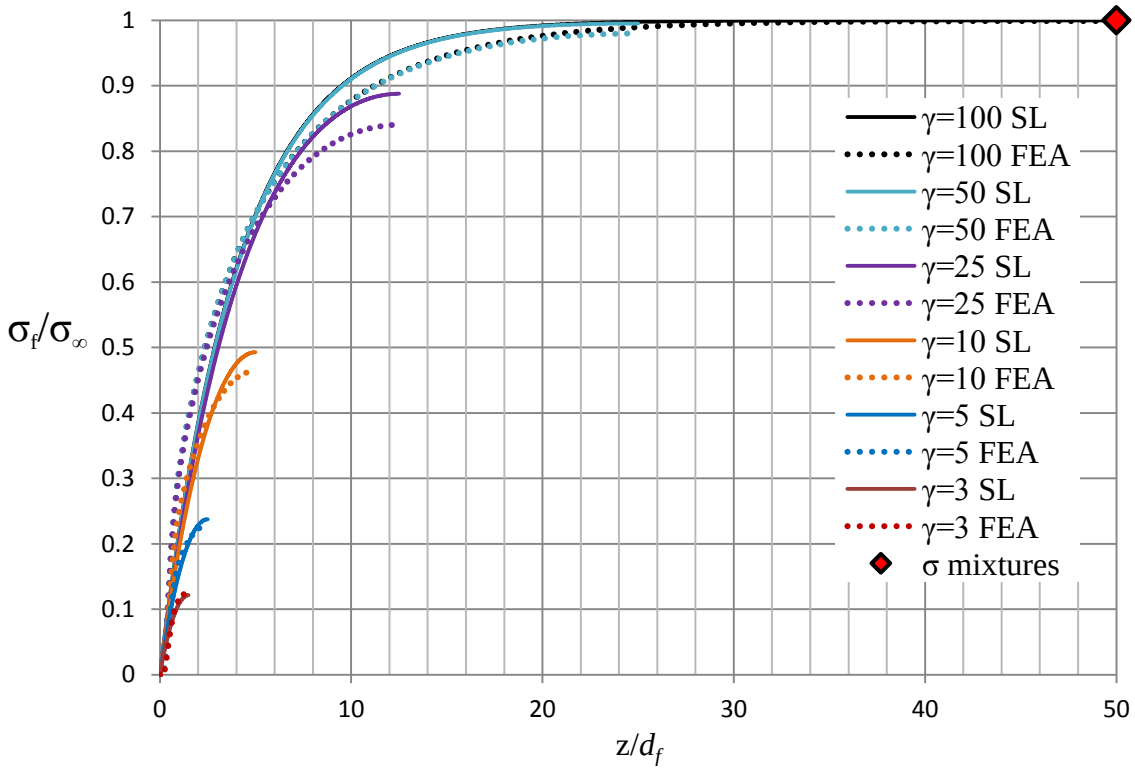

Figure 24. Average axial stress for fully embedded fibers of embedment lengths ranging from 3 to100d_f

The embedment length was set to 100 fiber diameters to study the effects of λ on the fitted value of *C*. A λ range of 10-200 was chosen specially to study the effects of Young's modulus on the fully embedded fiber configuration. By increasing the upper limit of λ, the behavior associated with stiff fibers *i.e.* carbon fibers could be observed. The embedment length of 100 fiber diameters ensured the composite would behave ideally over the full range of λ. The corresponding fitted values of *C* were plotted against λ and can be seen in figure 26. The axial stress is plotted against z in figure 27. As λ increases, the rate of change in *C* with respect to λ does not remain constant. However, the values do not converge even at value of λ=200.

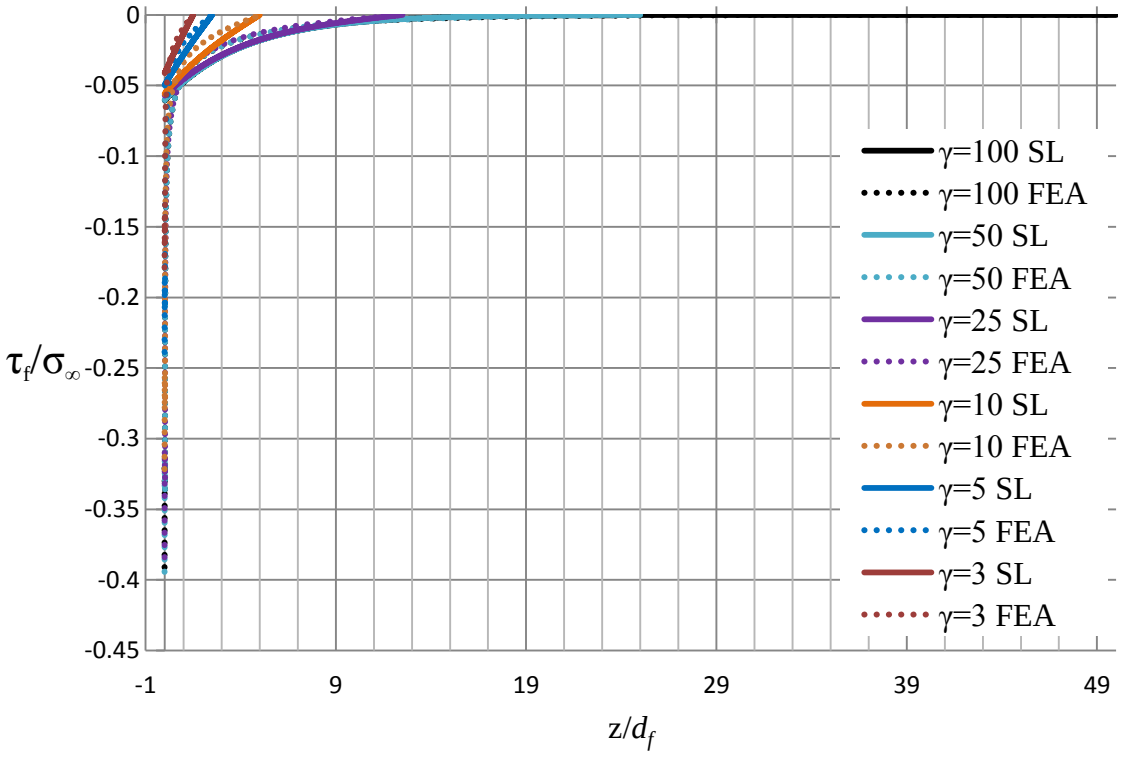

Figure 25. Shear stress for fully embedded fibers of embedment lengths ranging from 3 to 100d_f

Figure 27 suggests that at lower values of λ, load transfer to the fiber is completed at distances from the fiber ends much less than the critical fiber length. At λ=200, the stress becomes constant with location just before reaching the fiber center. As λ increases the rate at which the fiber can transfer its stress is reduced. For λ=200, the embedment length of 100 fiber diameters is just enough for the full transfer to take place. In this scenario the long fiber with a high Young's modulus behaves similarly to a shorter fiber with a lower Young's modulus.

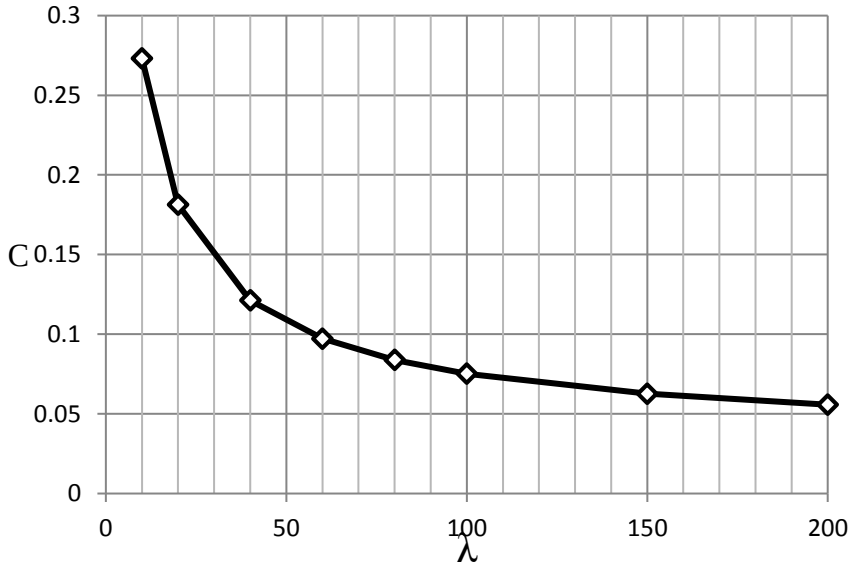

Figure 26. λ effect on *C* for a fully embedded fiber of $100d_f$

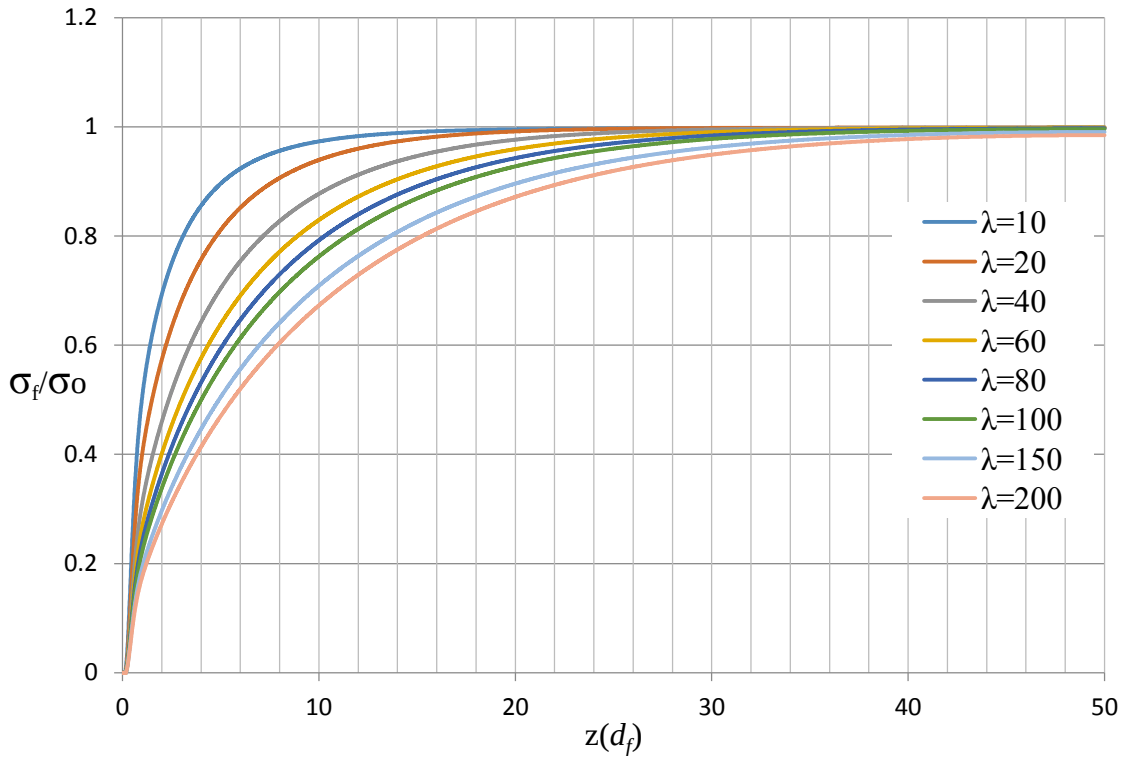

Figure 27. λ effect on stress behavior for a fully embedded fiber of $100d_f$

Chapter 8

Comparison to Experimental Data

Experimental results from various sources were used to validate the accuracy of β and therefore C. Microdroplet tests from Zhandarov *et al.* [24] and macrobond tests from Holsman *et al.* [26] were used to assess the results from the exposed fiber cases of both large and small embedment lengths. For the comparison of the first case of large embedment length, which approaches the behavior of an infinite embedment length, it is important to remember that the only parameter effecting C is the ratio of Young's modulus λ. The hole diameter α and embedment length γ were given values to reduce their effects on the induced fiber stress as much as possible. With that in mind when the plot of C vs λ for the infinite case is superimposed with data points for the finite cases of Zhandarov *et al.* and Holsman *et al.* there is agreement of the same order of magnitude and can be seen in figure 28. High accuracy was not expected considering Zhandarov *et al.*'s data was for specimens with various fiber treatments and the modeled specimen was created with a smooth fiber. Only the untreated specimen data from Holsman *et al.* was used in the comparison and was very close to the predicted value. Zhandarov *et al.*'s data was scattered for each value of λ. This can be attributed to the various fiber treatments involved altering the IFSS of the specimen along with the use of different fiber diameters.

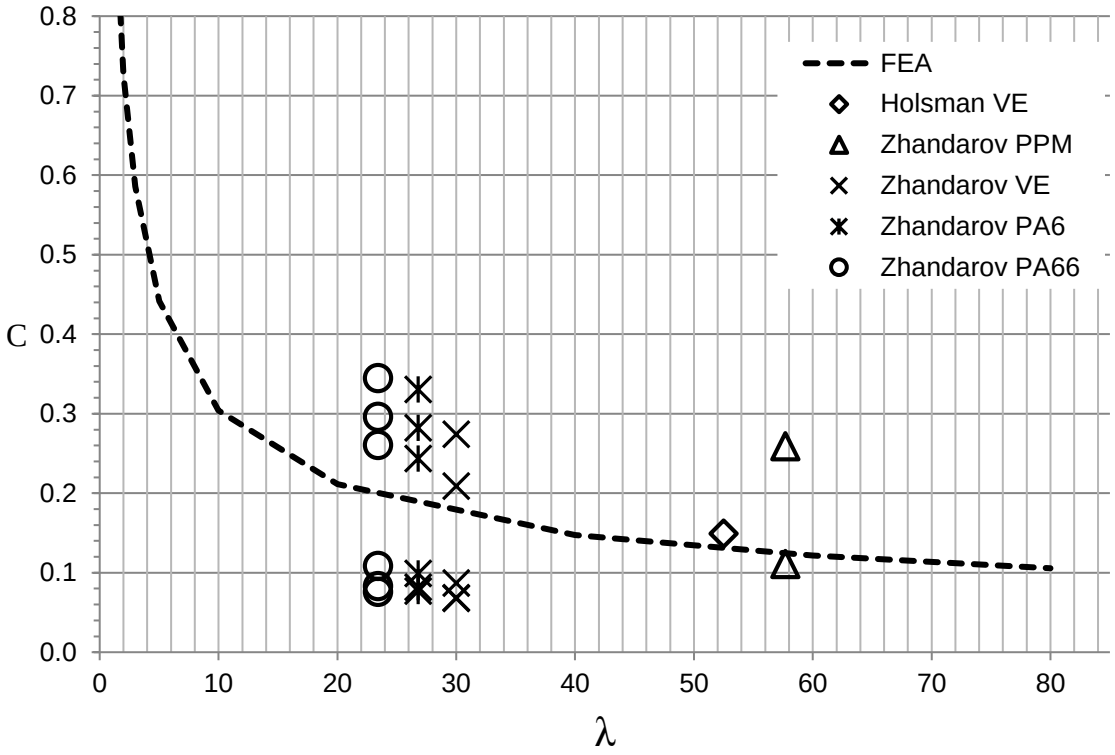

Figure 28. Numerically fitted values of *C* vs experimentally fitted values from Zhandarov *et al*. and Holsman *et al*.

The geometry of the macrobond test modeled was chosen for the purposes of recreating the experiment by Holsman *et al.* so that a more detailed validation could be achieved. Holsman et al., obtained a fitted value of C=0.149 to experimental data, whereas this study obtained a fitted value of C to numerical data, yielding an error of 11.4%. When α and γ were given values comparable to the test geometries of Holsman *et al.*'s experiments, the numerically predicted value of C increased by 30% for the 24 gauge fiber tests and 37% for the 28 gauge fiber tests. The different numerically predicted C values result from the change in fiber diameter for a constant hole size of the experiments, which results in different normalize hole sizes.

The effects from the change in α were further analyzed by creating finite element models for each specific data point from Holsman *et al.* and solving specific *C* values. These values of *C* were then used to solve for the ultimate interfacial shear strength for a single test explicitly, based on the expression for average shear strength at debond presented by Zhandarov *et al*. [24]. Using this approach, each combination of *C* and ultimate interfacial shear strength results in a unique curve relating average shear stress at failure to embedment length. As there were 7 experiments modeled, this approach results in 7 distinct curves, which are now superimposed onto the plot Holsman *et al*. used to establish a single best fit value of *C*. This comparison can be seen in figure 29.

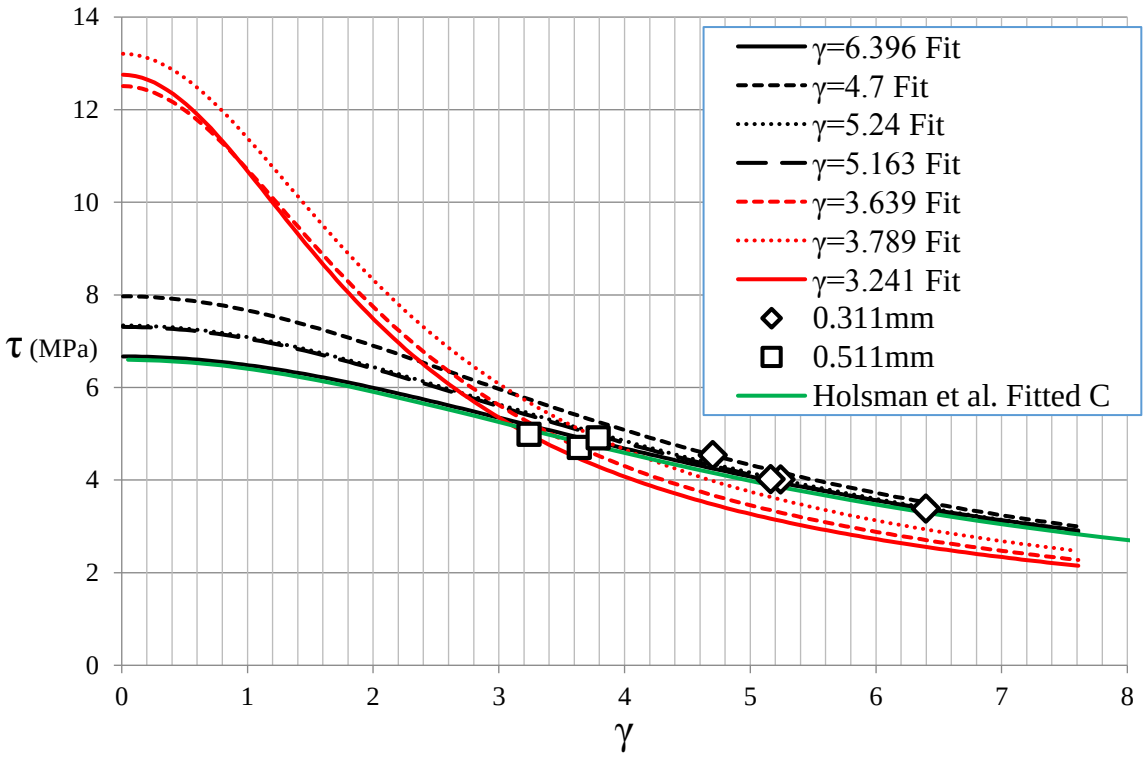

Figure 29. Holsman *et al.* vs SL shear stress curves

From figure 29 we can analyze incrementally how the geometric parameters affect the fitted value of *C* and the associated shear stress curves. The black data series represent the 0.312mm fibers used in the experiments from Holsman *et al*. They allow a hole diameter of approximately $2d_f$. The largest value of γ for the macrobond specimens is 6.396 which represents 2/3 of the length required for infinite behavior. These parameters allow for good agreement with the average shear stress curve fitted to 7 experimental test results by Holsman *et al*. However, as γ decreases the numerically predicted value of *C* increases and diverges from the experimental results even though there is no change in α. The larger (0.511mm) fibers result in a hole diameter of $1.24d_f$. Numerical simulations predict that the resulting *C* is sensitive to hole size in this range, due to stress concentrations that appear at low values of α. The significant variation in the plots, compared to the single best fit value obtained by Holsman *et al*. suggests that the numerical model predicts a greater sensitivity to hole size than actually occurrs in experiments. It is possible that issues with irregular contact in the experiments results in an effective hole diameter that is greater than the physical size of the actual hole in terms of load transfer.

Experimental results from Galiotis *et al*. [13] were used for the validation for the fully embedded fiber configuration. The FEA was conducted with the test geometries used by Galiotis *et al*. and an initial strain instead of an initial stress was used to simulate the fracture experiment. The rule of mixtures [34] was used to calculate the axial stress in the fiber by using numerical strain values pulled from the FEA. The fitted β value was calculated to be $0.0304\mu m^{-1}$ compared to the experimentally calculated value of $0.0192\mu m^{-1}$. One reason for the difference in values is that the material properties of the

experiment were not explicitly mentioned by Galiotis *et al*. Values for material properties were obtained from handbooks. A difference in λ could then have a large impact on the fitted value of *C*.

Chapter 9

Summary

In this thesis we analyzed three different cases of fiber pull out scenarios. First we looked at exposed fibers with a relatively infinite embedment length and hole diameter, then exposed fibers with finite embedment length and hole diameters, and finally fully embedded fibers. For the case of infinite embedment length multiple boundary conditions were studied along with two different methods of optimizing *C*. From the first case we observed that the optimized value of *C* is very sensitive to boundary conditions and how it is optimized for scenarios where the ratio of Young's modulus is less than 10. For values of λ greater than 10, the fitted values of *C* for each boundary condition and optimization method become similar. Most experiments dealing with fiber composites will have λ greater than10. For the case of infinite embedment length the only parameter affecting the value of *C* was λ. The parameters α and γ had minimal effects on the initial shear stress along the fiber/matrix interface. Therefore, when *C* was plotted against values of λ, the values were in good agreement with experimental data published by Zhandarov *et al.* and especially by Holsman *et al*. Data from Zhandarov *et al.* was scattered around the predicted values of *C*, which could be caused by the different fiber diameters and fiber treatments used for each value of λ. However, the average *C* value of each value of λ is in very good agreement with predicted values.

For the case of finite embedment length, embedment length along with the size of the hole the fiber was being pulled through were studied using a wide range of values.

The effects of α and γ on the fitted value of *C* were studied. There is a large stress concentration at the initial matrix surface for low values of α and γ. Through this method it was observed that values of *C* are fairly constant for values of γ greater than 10. However, there is no reasonable value of α above which fitted values of C become constant. The effect of λ on both α and γ was also studied. The slope of *C* vs λ was similar to the infinite embedment length case. As the values for α were reduced from an infinite case the plots of *C* vs γ increased in magnitude while the slope remained fairly constant. Changes in γ had a similar behavior along with a noticeable stress concentration at the fiber end for small values of γ.

Experiments from Holsman *et al.* were modeled using the approach developed for finite embedment length specimens. The goal was to observe the individual stress curves with specifically fitted *C* values bracketing the experimentally fitted stress curve publish by Holsman *et al*. The stress curves for the smaller fiber diameter behaved this way, but there was a large disagreement in ultimate shear strength when the larger fiber diameter fibers were modeled. The larger fiber diameter specimens had a smaller embedment length and a relatively small hole diameter. These two parameters drastically increased the initial shear stress in the fiber and therefore increase the fitted value of *C*. This behavior contradicts the behavior observed by Holsman *et al.* and one hypothesis is that imperfections in the geometry of the matrix material could affect the effective hole diameter for the purposes of load transfer. In this sense the effective experimental value of α may differ from the idealized value used for numerical simulations.

Minimizing errors in shear stress was found to be a poor means to obtain a fitted value of *C* for fully embedded fibers with short embedment lengths. As the geometry

moved away from being an idealized long fiber, the shear lag solution for the midplane stress in the fiber fell short of the numerical solution. To solve this problem the axial stress along the fiber's axis of symmetry was used in a least squares fit for optimizing β. The far field stress could be analytically calculated by modeling a long fiber and using the rule of mixtures to find the midplane stress in the fiber. Once this stress was calculated it allowed for the prediction of average axial stress in fibers ranging in length from 3 fiber diameters to 100 fiber diameters with good agreement for all scenarios. The fitted C values for the range of embedment lengths were slightly scattered in the area of γ=25 but still followed a trend in the sense that the value of C converged after an embedment length of 50 fiber diameters. A range of λ was also studied for the case of γ=100. The behavior of C affected by λ was similar to that of the exposed fiber cases. It was also observed that for very large values of λ the rate of stress transfer was slow enough for the composite to simulate the geometry of a short fiber composite even though it had an embedment length of 100 fiber diameters.

Chapter 10

Conclusions

Shear lag solutions with fitted values of β are able to capture the overall behavior of fiber pull out configurations that were identified by FEA solutions. Through the use of slightly different boundary conditions, both single exposed fiber and fully embedded fiber configurations can be modeled by the shear lag solutions. The effectiveness of methods used to optimize β proved to be case specific. Optimization using shear stress and strain energy per unit volume allowed for a best fit in most scenarios. Using average axial stress for minimizing errors in the shear lag solution resulted in better agreement with the FEA solution for midfiber stress for embedded fibers with short embedment lengths.

Predicted values of β were found to be of the same order of magnitude as experimentally fitted values. Better agreement was observed when the numerical model had large values of γ and α. The behavior of predicted β values was also observed to be similar to experimentally observed behavior through the use of Raman spectroscopy. This behavior was further validated when the effects of λ on β were in agreement with published results.

A difference in the sensitivity to different parameters was observed between the idealized modeled behavior and experimental behavior. Numerically fitted values of C were observed to be sensitive to changes in γ and α once they reached a specific lower limit. This behavior was not experimentally observed by Holsman *et al.*

Even though the modeled behavior of the experiment by Holsman *et al.* did not fully agree with the experimental results, the study of the material and geometric parameters involved in the creation of pull out tests can give us insight towards how to create future tests. This insight can allow us retool our experiments to isolate and better understand these effects with the goal of increasing the accuracy in which we measure IFSS. One example would be to use large values of α to reduce the initial stress concentration in a pull-out specimen, allowing more focus to be placed on the IFSS of the composite. More consideration into the preparation of sample is also suggested by the results discussed in this thesis.

Improved understanding of the load transfer of single fiber pullout configurations is a step toward micromechanical effects to models for fiber/matrix interface behavior. In addition to enabling the development of these models, improved test geometries facilitated by improved understanding of load transfer will be needed to validate the models.

References

[1] R. Day, K. Hewson, and P. Lovell, "Surface modification and its effect on the interfacial properties of model aramid-fibre/epoxy composites," *Composites Science and Technology*, vol. 62, no. 2, pp. 153–166, 2002.

[2] Y. F. Fu, K. Xu, J. Li, Z. Y. Sun, F. Q. Zhang, and D. M. Chen, "The Influence of Plasma Surface Treatment of Carbon Fibers on the Interfacial Adhesion Properties of UHMWPE Composite," *Polymer-Plastics Technology and Engineering*, vol. 51, no. 3, pp. 273–276, 2012.

[3] H. Li, H. Liang, F. He, Y. Huang, and Y. Wan, "Air dielectric barrier discharges plasma surface treatment of three-dimensional braided carbon fiber reinforced epoxy composites," *Surface and Coatings Technology*, vol. 203, no. 10-11, pp. 1317–1321, 2009.

[4] B. Miller, P. Muri, and L. Rebenfeld, "A microbond method for determination of the shear strength of a fiber/resin interface," Composites Science and Technology, vol. 28, no. 1, pp. 17–32, 1987.

[5] M. Nishikawa, T. Okabe, K. Hemmi, and N. Takeda, "Micromechanical modeling of the microbond test to quantify the interfacial properties of fiber-reinforced composites," *International Journal of Solids and Structures*, vol. 45, no. 14-15, pp. 4098–4113, 2008.

[6] H. Cen, Y. Kang, Z. Lei, Q. Qin, and W. Qiu, "Micromechanics analysis of Kevlar-29 aramid fiber and epoxy resin microdroplet composite by Micro-Raman spectroscopy," *Composite Structures*, vol. 75, no. 1-4, pp. 532–538, 2006.

[7] M. Piggott and S. Dai, "Debonding and friction at fibre-polymer interfaces. II: Macroscopic model experiments," *Composites Science and Technology*, vol. 31, no. 1, pp. 15–24, 1988.

[8] A. Takaku and R. G. C. Arridge, "The effect of interfacial radial and shear stress on fibre pull-out in composite materials," Journal of Physics D: Applied Physics J. Phys. D: Appl. Phys., vol. 6, no. 17, pp. 2038–2047, 1973.

[9] L. P. Hann and D. E. Hirt, "Simulating the microbond technique with macrodroplets," Composites Science and Technology, vol. 54, no. 4, pp. 423–430, 1995.

[10] K.-H. Tsai and K.-S. Kim, "The micromechanics of fiber pull-out," *Journal of the Mechanics and Physics of Solids*, vol. 44, no. 7, pp. 1147–1177, 1996.

[11] J. Brandstetter, K. Kromp, H. Peterlik, and R. Weiss, “Measurement of shear lag parameter β for a fibre bundle pull-out geometry,” *Composites Science and Technology*, vol. 64, no. 1, pp. 65–70, 2004.

[12] D. Bannister, M. Andrews, A. Cervenka, and R. Young, “Analysis of the single-fibre pull-out test by means of Raman spectroscopy: Part II. Micromechanics of deformation for an aramid/epoxy system,” *Composites Science and Technology*, vol. 53, no. 4, pp. 411–421, 1995.

[13] C. Galiotis and C. Galiotis, “Definition and measurement of the shear-lag parameter, β, as an index of the stress transfer efficiency in polymer composites,” *Journal of Materials Science*, vol. 33, no. 5, pp. 1137–1143, 1998.

[14] I. D. Wolf, “Micro-Raman spectroscopy to study local mechanical stress in silicon integrated circuits,” *Semiconductor Science and Technology Semicond. Sci. Technol.*, vol. 11, no. 2, pp. 139–154, Jan. 1996.

[15] L.-M. Zhou, J.-K. Kim, and Y.-W. Mai, “Micromechanical characterisation of fibre/matrix interfaces,” *Composites Science and Technology*, vol. 48, no. 1-4, pp. 227–236, 1993.

[16] J. A. Nairn, “On the use of shear-lag methods for analysis of stress transfer in unidirectional composites,” *Mechanics of Materials*, vol. 26, no. 2, pp. 63–80, 1997.

[17] S. F. Zhandarov, E. Mäder, and O. R. Yurkevich, “Indirect estimation of fiber/polymer bond strength and interfacial friction from maximum load values recorded in the microbond and pull-out tests. Part I: local bond strength,” *Journal of Adhesion Science and Technology*, vol. 16, no. 9, pp. 1171–1200, 2002.

[18] S. Zhandarov, E. Pisanova, and E. Mäder, “Is there any contradiction between the stress and energy failure criteria in micromechanical tests? Part III. Experimental observation of crack propagation in the microbond test,” *Journal of Adhesion Science and Technology*, vol. 19, no. 8, pp. 679–704, 2005.

[19] P. Zhao and S. Ji, “Refinements of shear-lag model and its applications,” *Tectonophysics*, vol. 279, no. 1-4, pp. 37–53, 1997.

[20] T. Lacroix, B. Tilmans, R. Keunings, M. Desaeger, and I. Verpoest, “Modelling of critical fibre length and interfacial debonding in the fragmentation testing of polymer composites,” *Composites Science and Technology*, vol. 43, no. 4, pp. 379–387, 1992.

[21] H. L. Cox, “The elasticity and strength of paper and other fibrous materials,” *Br. J. Appl. Phys. British Journal of Applied Physics*, vol. 3, no. 3, pp. 72–79, 1952.

[22] Nayfeh, A. H., 1977, *"Thermochanically Induced Interfacial Stresses in Fibrous Composites," Fibre Science and Technology*, 10: 195-205.

[23] Z. Xia, T. Okabe, and W. Curtin, "Shear-lag versus finite element models for stress transfer in fiber-reinforced composites," *Composites Science and Technology*, vol. 62, no. 9, pp. 1141–1149, 2002.

[24] S. Zhandarov, E. Pisanova, E. Mäder, and J. A. Nairn, "Investigation of load transfer between the fiber and the matrix in pull-out tests with fibers having different diameters," *Journal of Adhesion Science and Technology*, vol. 15, no. 2, pp. 205–222, 2001.

[25] C. H. Marotzke, "Influence of the fiber length on the stress transfer from glass and carbon fibers into a thermoplastic matrix in the pull-out test," Compos. Interfaces, vol. 1, no. 2, pp. 153–166, Jan. 1993.

[26] N. E. Holsman, B. A. Holford, J. A. Wesley, K. W. Wynn, and W. T. Riddell, "Modification of Fiber-Matrix Bond Strength through Surface Treatments," *Proceedings of the American Society for Composites 2014 Twenty-ninth Technical Conference on Composite Materials*, vol. 29, pp. 19–47, 2014.

[27] J. W. Hutchinson and H. M. Jensen, "Models of fiber debonding and pullout in brittle composites with friction," *Mechanics of Materials*, vol. 9, no. 2, pp. 139–163, 1990.

[28] G. Lin, P. Geubelle, and N. Sottos, "Simulation of fiber debonding with friction in a model composite pushout test," *International Journal of Solids and Structures*, vol. 38, no. 46-47, pp. 8547–8562, 2001.

[29] J. Tsai, A. Patra, and R. Wetherhold, "Finite element simulation of shaped ductile fiber pullout using a mixed cohesive zone/friction interface model," *Composites Part A: Applied Science and Manufacturing*, vol. 36, no. 6, pp. 827–838, 2005.

[30] Q.-S. Yang, Q.-H. Qin, and X.-R. Peng, "Size effects in the fiber pullout test," *Composite Structures*, vol. 61, no. 3, pp. 193–198, 2003.

[31] C. Marotzke, "The elastic stress field arising in the single-fiber pull-out test," *Composites Science and Technology*, vol. 50, no. 3, pp. 393–405, 1994.

[32] V. Bheemreddy, K. Chandrashekhara, L. Dharani, and G. Hilmas, "Modeling of fiber pull-out in continuous fiber reinforced ceramic composites using finite element method and artificial neural networks," *Computational Materials Science*, vol. 79, pp. 663–673, 2013.

[33] W. Chen, Zourong; Yan, "A Shear-Lag model with a cohesive fibre-matrix interface for analysis of fibre pull-out," *Mech. Mater.*, vol. 91, pp. 119–135, 2015.

[34] W. D. Callister, *Fundamentals of materials science and engineering: an integrated approach*. Hoboken, NJ: John Wiley & Sons, 2005.

[35] P. Herrera-Franco and L. Drzal, "Comparison of methods for the measurement of fibre/matrix adhesion in composites," *Composites*, vol. 23, no. 1, pp. 2–27, 1992.

[36] G. Avery and W. T. Riddell, "A Bridge between Finite Element and Shear Lag Analyses for Fiber Pull Out," *Proceedings of the American Society for Composites 2015 Thirtieth Technical Conference on Composite Materials*, vol. 30, pp. 1688, 2015.